Brown Carbon Fuel and Emission Source Attributions to Global Snow Darkening Effect

Hunter Brown[1], Hailong Wang[2], Mark Flanner[3], Xiaohong Liu[4], Balwinder Singh[5], Rudong Zhang[5], Yang Yang[6], and Mingxuan Wu[2]

[1]University of Wyoming, Texas A&M University
[2]Pacific Northwest National Laboratory
[3]University of Michigan-Ann Arbor
[4]Texas A&M University
[5]Pacific Northwest National Laboratory (DOE)
[6]Nanjing University of Information Science and Technology

November 24, 2022

Abstract

Snow and ice albedo reduction due to deposition of absorbing particles (i.e., snow darkening effect (SDE)) warms the Earth system and is largely attributed to black carbon (BC) and dust. Absorbing organic aerosol (BrC) also contributes to SDE but has received less attention due to uncertainty and challenges in model representation. This work incorporates the SDE of absorbing organic aerosol (BrC) from biomass burning and biofuel sources into the Snow Ice and Aerosol Radiative (SNICAR) model within a variant of the Community Earth System Model (CESM). Additionally, 12 different emission regions of BrC and BC from biomass burning and biofuel sources are tagged to quantify the relative contribution to global and regional SDE. BrC global SDE (0.021–0.056 Wm^{-2}) is larger than other model estimates, corresponding to 37%–98% of the SDE from BC. When compared to observations, BrC simulations have a range in median bias (-2.5%–+21%), with better agreement in the simulations that include BrC photochemical bleaching. The largest relative contributions to global BrC SDE are traced to Northern Asia (23%–31%), Southeast Asia (16%–21%), and South Africa (13%–17%). Transport from Southeast Asia contributes nearly half of the regional BrC SDE in Antarctica (0.084–0.3 Wm^{-2}), which is the largest regional input to global BrC SDE. Lower latitude BrC SDE is correlated with snowmelt, in-snow BrC concentrations, and snow cover fraction, while polar BrC SDE is correlated with surface insolation and snowmelt. This indicates the importance of in-snow processes and snow feedbacks on modeled BrC SDE.

Hosted file

`essoar.10507836.1.docx` available at https://authorea.com/users/552441/articles/604755-brown-carbon-fuel-and-emission-source-attributions-to-global-snow-darkening-effect

Hunter Brown[1,2], Hailong Wang[3], Mark Flanner[4], Xiaohong Liu[2], Balwinder Singh[3], Rudong Zhang[3], Yang Yang[5], Mingxuan Wu[3]

[1]Department of Atmospheric Science, University of Wyoming, Laramie, WY, USA.

[2]Department of Atmospheric Sciences, Texas A&M University, College Station, TX, USA.

[3]Atmospheric Sciences and Global Change Division, Pacific Northwest National Laboratory, Richland, WA, USA.

[4]Department of Atmospheric, Oceanic and Space Sciences, University of Michigan, Ann Arbor MI, USA

[5]Jiangsu Key Laboratory of Atmospheric Environment Monitoring and Pollution Control, Jiangsu Collaborative Innovation Center of Atmospheric Environment and Equipment Technology, School of Environmental Science and Engineering, Nanjing University of Information Science and Technology, Nanjing, Jiangsu, China

Corresponding authors: Hailong Wang (hailong.wang@pnnl.gov) and Xiaohong Liu (xiaohong.liu@tamu.edu)

Key Points:

- Brown carbon forcing on snow is larger than in previous modeling studies and is comparable to the snow darkening effect of black carbon.
- Northern Asia, Southeast Asia, and Southern Africa are the largest source contributors to global brown carbon snow darkening effect.
- Seasonal brown carbon is closely correlated with snow processes in the model, indicating the importance of aerosol-snow feedbacks.

Abstract

Snow and ice albedo reduction due to deposition of absorbing particles (i.e., snow darkening effect (SDE)) warms the Earth system and is largely attributed to black carbon (BC) and dust. Absorbing organic aerosol (BrC) also contributes to SDE but has received less attention due to uncertainty and challenges in model representation. This work incorporates the SDE of absorbing organic aerosol (BrC) from biomass burning and biofuel sources into the Snow Ice and Aerosol Radiative (SNICAR) model within a variant of the Community Earth System Model (CESM). Additionally, 12 different emission regions of BrC and BC from biomass burning and biofuel sources are tagged to quantify the relative contribution to global and regional SDE. BrC global SDE (0.021–0.056 Wm^{-2}) is larger than other model estimates, corresponding to 37%–98% of the SDE from BC. When compared to observations, BrC simulations have a range in median bias (-2.5%–+21%), with better agreement in the simulations that include BrC photochemical bleaching. The largest relative contributions to global BrC SDE are traced to Northern Asia (23%–31%), Southeast Asia (16%–21%), and South

Africa (13%–17%). Transport from Southeast Asia contributes nearly half of the regional BrC SDE in Antarctica (0.084–0.3 Wm^{-2}), which is the largest regional input to global BrC SDE. Lower latitude BrC SDE is correlated with snowmelt, in-snow BrC concentrations, and snow cover fraction, while polar BrC SDE is correlated with surface insolation and snowmelt. This indicates the importance of in-snow processes and snow feedbacks on modeled BrC SDE.

Plain Language Summary

Bright surfaces like snow and ice reflect some of the sun's light back to space, leading to less surface warming. These reflective surfaces can be coated by light absorbing particles such as soot and dust, reducing their reflectivity and speeding up the warming of the climate. "Brown carbon" is another absorbing particle that also darkens these surfaces. Fewer studies have looked at this climate effect due to challenges in modeling brown carbon in the atmosphere and on snow. Here, a more detailed treatment of brown carbon from fires is added to a global climate model to understand how brown carbon affects snow reflectivity. This model also keeps track of where the brown carbon in smoke is released to understand how different parts of the world impact snow surfaces. One of the main findings of this work is that brown carbon is better at darkening snow surfaces than previous work has shown. When compared to soot–which is the strongest snow darkening agent–brown carbon has a comparable effect, ranging from around half to the same darkening of snow surfaces as soot. Additionally, brown carbon from large fires in close proximity to snow has largest impacts on snow reflectivity.

1 Introduction

Reduction of surface albedo of snow and ice due to absorbing aerosol deposition reduces the global cooling effect of these reflective surfaces (Clarke & Noone, 1985; Warren & Wiscombe, 1980). This "snow darkening effect" (SDE) increases the energy stored in the Earth system while also leading to a number of positive feedbacks that can accelerate snowmelt. There is high confidence that the reduced snow cover at lower elevations and global glacial recession are attributed to increasing global surface temperatures and subsequent increases in liquid precipitation (Hock et al., 2019). Compounding these effects are the feedbacks associated with SDE, which have been correlated with earlier snow and glacier melt, reduced snow cover, decreased snow-water equivalent, and negative ice-sheet mass-balance (Painter et al., 2007; Rahimi et al., 2019, 2020; Skiles et al., 2012; Tedesco et al., 2011; C. Wu et al., 2018). Uncertainties still exist in estimations of SDE, and improving the representation of SDE in climate models can help clarify the future implications of reductions in the Earth's cryosphere. These include increasing temperature in historically snow and ice covered regions (Boucher et al., 2013), sea level rise (Hugonnet et al., 2021; Nerem et al., 2018), and impacts on population centers that depend on mountain snowpack for water and power (Jiao et al., 2014; D. Liu et al., 2020); Meredith et al., 2019; Hock et al., 2019).

A variety of light-absorbing particles (LAPs) are responsible for this SDE including dust, soot (black carbon (BC)), and absorbing organic carbon (brown carbon (BrC)). The degree to which these LAPs impact snow and ice albedo, and therefore the climate, is still uncertain due to the challenges in modeling atmospheric aerosol lifecycle (Jiao et al., 2014; D. Liu et al., 2020), aerosol optical properties (Brown et al., 2021; C. He et al., 2015; Potenza et al., 2016; Saleh, 2020), and aerosol processing and feedbacks within snowpack (Flanner et al., 2012; He et al., 2018a, 2018b; Schwarz et al., 2013). BC is considered the greatest snow albedo forcing agent, with a forcing "efficacy" (i.e., the change in global mean temperature per unit radiative forcing (Hansen et al., 2005)) ~2-4 times that of CO_2 (Bond et al., 2013; Flanner et al., 2007; Hansen et al., 2007). BC is directly emitted (i.e., a primary aerosol) into the atmosphere from high temperature flaming combustion of anthropogenic and natural sources. It absorbs strongly in all wavelengths of visible light (i.e., weak wavelength dependence), has a high vaporization temperature (4000 $^\circ$ K), and is insoluble in water and organic solvents (Bond et al., 2013). When compared to dust, BC is ~50 times more absorbing per unit mass (Warren, 1984), but the SDE due to dust can exceed that of BC in regions more influenced by dust deposition (e.g., San Juan Mountains, Colorado and the Tibetan Plateau (Ming et al., 2013; Painter et al., 2007)). Fewer studies have estimated the impact of BrC, but measurements suggest that it may contribute as much as 20-50% of the particulate absorption on the surface of snow (Doherty et al., 2010) and may dominate the non-BC LAP contribution to SDE in the Arctic (Hegg et al., 2010). Furthermore, an increasing trend in organic carbon (OC) mass concentrations and increasing OC to BC mass ratio in ice cores dating back to 1990 suggest an increasing impact on SDE from BrC (M. Wang et al., 2015; Xu et al., 2009). While co-emitted from many of the same combustion sources as BC, BrC has a more complex set of defining characteristics.

The term "brown carbon" describes a vast collection of light absorbing organic aerosol species directly emitted from lower temperature combustion conditions and formed via atmospheric chemical reactions (i.e., secondary organic aerosol (SOA)). These tend to absorb weakly in longer visible wavelengths but exhibit a sharp increase in absorption at short visible and UV wavelengths (i.e., strong wavelength dependent absorption) (Laskin et al., 2015; Saleh, 2020). That being said, the optical properties, hygroscopicity, and volatility of BrC differ greatly depending on the fuel source and the burn conditions (Saleh et al., 2014). This has led to evidence of a BrC continuum (Adler et al., 2019; Saleh et al., 2018) ranging from higher wavelength dependence/higher solubility/higher volatility BrC species (e.g., secondary BrC), to lower wavelength dependence/lower solubility/lower volatility primary BrC species more similar to BC (Saleh, 2020). Additionally, the light absorption of BrC in the atmosphere can change over time, both decreasing due to photochemical oxidation and bleaching (Forrister et al., 2015; de Sá et al., 2019; X. Wang et al., 2016) and stabilizing/increasing due to nitrogen driven reactions (Li et al., 2020; P. Lin et al., 2017; Zhong & Jang, 2014).

Observations of LAP mass and absorption in snow are challenged by aerosol compositional diversity and measurement sensitivity. The climatically relevant reductions in snow albedo due to SDE tend to be below satellite detection limits (e.g., 1-3% reduction in snow albedo in the Arctic due to soot (Clarke & Noone, 1985)), and it is difficult to differentiate LAP effects from other environmental conditions that impact remotely measured surface albedo such as patchy snow, blowing snow, and thin cloud cover (Warren, 2013). This rules out remote sensing as a viable means of measuring large scale SDE with the exception of high impact deposition events (Gautam et al., 2013; Painter et al., 2012). The common approach is to measure the mass concentration and absorption of particles collected on filters from melted snow samples. The use of spectrally resolved absorption of aerosols on filters conveys information about the broadband aerosol absorption in snow as well as the relative fractions of different species in snow. Due to the low spatial coverage of these samples, chemical transport models (CTM) and Earth system models (ESM) provide valuable tools for estimating the global aerosol contributions to, and the global climate impact of, SDE due to LAPs.

Models have evolved from simplified representations of SDE that applied fixed albedo reductions for BC over large global regions (Hansen & Nazarenko, 2004) to simulations that include additional species and in-snow post-depositional processes. The most advanced land and sea-ice models include snow feedback effects such as grain size evolution and changes in snow surface sublimation (Flanner et al., 2007, 2009; Koch et al., 2009), surface retention of hydrophobic aerosol due to melt (Flanner et al., 2007, 2009; Qian et al., 2014; Skeie et al., 2011), inclusion of in-snow dust (Flanner et al., 2009; Jacobson, 2012; Yasunari et al., 2014) and BrC (Jacobson, 2012; G. Lin et al., 2014; Tuccella et al., 2021; Yasunari et al., 2014); and consideration of polydisperse BC within ice grains (Flanner et al., 2012; C. He et al., 2018a, 2018b; H. Wang et al., 2020).

Within the literature, there are a many values for LAP SDE with a variety of assumptions made. Some values are reported as a radiative forcing (RF), which can be either an anthropogenic forcing (i.e., differences between preindustrial and present-day top of the atmosphere (TOA) flux, with and without consideration of LAP on snow), or the difference in present-day TOA flux after allowing the atmosphere to reach some equilibrium state with the LAP surface albedo perturbation. Furthermore, some modeling studies only report LAP SDE over land snow and ice, while others include the LAP induced albedo reduction of sea ice. Recent studies estimate present-day global BC SDE that range from 0.033 Wm^{-2} (Tuccella et al., 2021) to 0.037 Wm^{-2} (Lawrence et al., 2012), and anthropogenic BC SDE that ranges from 0.04 (0.02–0.09) Wm^{-2} (Boucher et al., 2013) to 0.14 (0.04–0.34) Wm^{-2} (Bond et al., 2013). Dust SDE has received less attention due to its lower absorption and uncertainties in modeling emissions and optical properties, but present-day global dust SDE are estimated at 0.012-0.36 Wm^{-2} (Lawrence et al., 2012; Tuccella et al., 2021). While BC and dust are becoming more common in simulations of SDE, less confidence is attributed to BrC estimates of SDE, with current global estimates putting present-day BrC

SDE at a range of 0.0022 – 0.0066 Wm^{-2} (Tuccella et al., 2021) and anthropogenic BrC SDE at a range of 0.0011-0.0031 Wm^{-2} (G. Lin et al., 2014). There is also evidence that LAPs influence the SDE of one another by changing the snow grain sizes and surface albedo over which the SDE are calculated. For example, the presence of dust can reduce BC SDE by 10–40% (Bond et al., 2013; Flanner et al., 2009) and the presence of BrC on clean snowpack can have twice the radiative impact of BrC deposited on a snow surface with other impurities (Beres et al., 2020).

Aerosol tagging methods similar to that used in this work have been applied extensively to address aerosol forcing and long-term trends over distinct global regions. These include the Arctic (Ren et al., 2020; H. Wang et al., 2014), China (Yang et al., 2017; Yang et al., 2018a), United States (Yang et al., 2018b) and Europe (Yang et al., 2020). In addition to source tagging, this approach has also been used to understand emission sector (i.e., fossil fuels (FF), BB, BF) contributions to aerosol burden and radiative forcing over the Tibetan Plateau (Zhang et al., 2015b) and western North America (Zhang et al., 2015a).

This work utilizes the Community Earth System Model (CESM) to present the first quantification of BrC SDE that includes temporal and spatial variation of BrC refractive index (RI) from varying source emissions and photochemical bleaching (Saleh et al., 2014; X. Wang et al., 2018). This is accomplished by adding deposition of BrC originating from BB and BF emission sectors with a RI that depends on fuel type and undergoes photochemical bleaching (Brown et al., 2018) to the Snow Ice and Aerosol Radiative (SNICAR; Flanner et al., 2007) model in CESM. The following sections validate our BrC implementation with surface observations, analyze the contributions to global SDE of BrC (with and without photochemical bleaching) from 12 global tagged source regions, and address the SDE impacts of BC and BrC in four major receptor regions in the Earth's cryosphere.

2 Model and Experiments

2.1 Model Description

This work uses the atmosphere component of version 1 of CESM, the Community Atmosphere Model version 5.4 (CAM5.4) (Hannay and Neale, 2015), coupled with the Community Land Model version 4 (CLM4) (Oleson et al., 2010) – the same CESM version used by Brown et al. (2018). The CAM5.4 includes a two-moment stratiform cloud microphysics scheme to predict cloud mass and number mixing ratios of liquid and ice (Morrison & Gettelman, 2008) and a prognostic precipitation scheme (Gettelman et al., 2015). Dust aerosol size and optical property treatments are as described in Albani et al. (2014). This study also uses the four-mode version of the Modal Aerosol Module (MAM4) (X. Liu et al., 2016), where the lognormal modes are defined and referenced herein as: Aitken (0.015–0.053 m, = 1. 8), accumulation (0.058–0.27 m, = 1. 6), coarse (0.80–3.65 m, = 1. 8), and primary carbon (0.039–0.13 m, = 1. 6) modes. Within CLM4, the Snow, Ice, and Aerosol Radiative (SNICAR) model

is activated, which calculates changes in land-surface snow albedo due to BC and dust deposition as well as the resulting feedbacks that affect snow cover and snow grain size (Flanner et al., 2007, 2009).

2.2 Model Modifications

2.2.1 Treatment of Atmospheric BrC

This study includes the representation of BrC in CAM5.4 based on the approach described in Brown et al. (2018), which treats all POA from BB and BF as BrC, neglecting the contributions from FF POA. The absorption of BrC is limited to wavelengths of light ranging from 304–1010 nm and is parameterized based on the grid-cell BC-to-POA ratio from BB and BF sources following Saleh et al. (2014). Brown et al. (2018) also includes an option of the photochemical bleaching effect of BrC, where the BrC half-life depends on the hydroxyl radical concentration ([OH]) in each grid cell (X. Wang et al., 2018). This assumption matches observed BrC absorption decay (Forrister et al., 2015; X. Wang et al., 2016), but likely overestimates the decay of BrC because the solvent extraction methods used to measure BrC absorption miss the insoluble fraction of BrC in samples (Saleh, 2020). As a result, the two simulations with and without BrC bleaching can be thought of as low and high bounds, respectively, of BrC absorption in the atmosphere. While POA from BB and BF sources is parameterized in this study, SOA is not explicitly treated as BrC and does not undergo photochemical bleaching. That being said, the default SOA imaginary RI (Hess et al., 1998) can be considered weakly absorbing BrC, roughly equivalent to measurements of BrC from smoldering biomass combustion and SOA from biomass combustion (Saleh, 2020).

2.2.2 Carbonaceous Aerosol Tagging

Regional carbonaceous aerosol emissions are tagged in this model in order to understand the contributions of BC and BrC to SDE from different fuel sectors and different emission source regions. The aerosol tagging modifications to the code are an extension of those used in a number of studies addressing BC and other aerosol transport and climate impacts (Ren et al., 2020; H. Wang et al., 2014; Yang et al., 2017, 2020; Yang et al., 2018a; Yang et al., 2018b; Zhang et al., 2015a; Zhang et al., 2015b). This work differs from the aforementioned studies in its tagging of POA in addition to BC. For BC and POA, emissions are separated into BB, BF, and FF emissions, where POA from BB and BF are treated as BrC. The BB and BF emissions for BC and BrC are further separated into 12 source regions (Fig. 1). Table 1 describes source and regional tags for BC and POA.

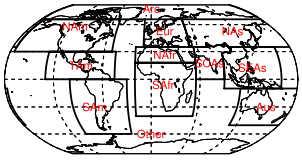

Figure 1: A depiction of the 12 different regions applied to POA and BC emissions from biomass burning and biofuel sectors in the aerosol tagging scheme. The region names are: Arctic (Arc), North America (NAm), Tropical America (TAm), South America (SAm), Europe (Eur), Northern Africa (NAfr), Southern Africa (SAfr), Northern Asia (NAs), South Central Asia (SCAs), Southeast Asia (SEAs), Australia (Aus), and all other island and oceanic emissions (Other).

Table 1: Description of the tagged carbonaceous aerosols (BC and POA) in the model simulations used in this study. Each tagged species is separated into three fuel sectors (biomass burning (BB), biofuel (BF), and fossil fuels (FF)). The BB and BF sectors are further separated into 12 regional tags that are defined in Fig. 1. For POA, the BB and BF sectors are treated as brown carbon (BrC) based on model implementation described in Brown et al. (2018).

Tagged Species	**Sector(s)**	**Source Region(s)**
BC	Biomass Burning (BB) Biofuel (BF)	Arctic (Arc) North America (NAm) Tropical America (TAm) South America (SAm) Europe (Eur) Northern Africa (NAfr) Southern Africa (SAfr) Northern Asia (NAs) South Central Asia (SCAs) Southeast Asia (SEAs) Australia (Aus) Island and oceanic emissions (Other)

Tagged Species	**Sector(s)**	**Source Region(s)**
BC	Fossil Fuel (FF)	Global
POA (BrC)	Biomass Burning (BB)	Arctic (Arc)
	Biofuel (BF)	North America (NAm)
		Tropical America (TAm)
		South America (SAm)
		Europe (Eur)
		Northern Africa (NAfr)
		Southern Africa (SAfr)
		Northern Asia (NAs)
		South Central Asia (SCAs)
		Southeast Asia (SEAs)
		Australia (Aus)
		Island and oceanic emissions (Other)
POA	Fossil Fuel (FF)	Global

2.2.3 Treatment of BrC in the SNICAR Model

To quantify the BrC contribution to SDE, CESM has to be modified to pass information about BrC deposition and RI from CAM5.4 to SNICAR (within the land component CLM) (note: SNICAR only calculates LAP SDE on land snow and ice). In CAM, aerosol species are separated into multiple, interactive size modes (X. Liu et al., 2012, 2016) while in SNICAR aerosol species are treated as either hygroscopic or hydrophilic particles for use in estimating meltwater scavenging efficiency (Flanner et al., 2007). This necessitates mass-weighting of the modal POA contributions to the BrC RI by source (BB and BF) and by region in CAM to ensure compatibility with CLM bulk organic aerosol (OC). Furthermore, differences in aerosol optical property calculations – online, parameterized Mie calculations in CAM versus offline, bulk aerosol optical property calculations in SNICAR – require additional steps to incorporate the temporally and spatially varied BrC optical properties into the SNICAR model. A brief description follows for how BrC is included in SNICAR, with a visual depiction of the process in Figure S1.

Modal aerosol must be converted to hydrophilic/hydrophobic OC in order to pass modal aerosol deposition flux from CAM to SNICAR. In the case of OC, this means that dry/wet deposition of cloud-borne and interstitial POA and SOA is converted into hydrophilic and hydrophobic OC. This is an issue when trying to parse out the BrC contribution to OC at the land surface, because only POA from BB and BF sources are treated as absorbing. To solve this problem, the bulk OC deposition flux is further separated into the following seven sources: hydrophobic POA (from BB, BF, and FF), hydrophilic POA

(from BB, BF, and FF), and hydrophilic SOA. This is done for each species and source following the assumptions currently used in CESM for the conversion of modal to bulk aerosols: interstitial accumulation mode aerosol and all cloud-borne aerosol are hydrophilic, while interstitial primary carbon mode aerosol is hydrophobic. Each of these fluxes can then be used to calculate mass-weighted contributions to OC optical properties.

Aerosol optical properties within CAM are calculated via parameterized Mie calculations for each aerosol species at each time step, wavelength band (14 shortwave and 16 longwave bands (0.2–12.195 µm and 3.08–1000.0 µm, respectively; Neale et al., 2012)), and grid-cell (Ghan & Zaveri, 2007). These calculations also take into account aerosol size and the assumption that aerosol species within each size mode are well-mixed internally (i.e., volume-weighted aerosol hygroscopicity and RI). For the SNICAR model, optical properties for in-snow LAPs are calculated offline using Mie calculations that assume a fixed size distribution and RI for each species. These optical properties are then calculated at wavelengths from 0.3 to 5.0 µm and spectrally weighted into 5 optical property bands (1 visible and 4 near-infrared).

The OC particles in SNICAR are a combination of BrC and non-absorbing sources of POA and SOA from CAM, and there is additional variation in the BrC RI depending on source and photochemical bleaching. Separation of BrC and non-absorbing OC in SNICAR is accounted for by weighting optical properties by deposition mass. The optical properties in question are a combined BB/BF BrC RI at 550 nm – scaled by modal and regional mass contributions from BB and BF – that is passed from CAM to SNICAR. Within SNICAR, a look-up table (LU-RI) is generated that encompasses the possible range in BrC RI based on possible ranges in emitted BC/POA (0.01–0.5) and photochemical bleaching coefficients (1.0–0.25) (Brown et al., 2018). The BrC RI from CAM is matched to LU-RI, generating an index within the table of possible BrC RI where the transferred value lies. Similar lookup tables (LU-OP) are generated for the offline calculations of BrC optical properties (i.e., aerosol mass extinction, asymmetry parameter, and single scattering albedo) that span the full range of values of BrC RI across the full spectrum in SNICAR (0.3–5.0 µm). The index of the BrC RI from CAM in the LU-RI is matched to that of LU-OP, giving an optical property that takes into account photochemical bleaching effects and variation in emission BC/POA ratio. Because this method relies on the possible range in BrC RI as opposed to direct comparison of aerosol optical properties, it is independent of the different wave band resolutions and different aerosol size treatments between CAM and SNICAR.

This raises the second issue faced in passing BrC to the SNICAR model, which is that CAM considers evolving aerosol size distributions in its calculations of aerosol optical properties, while SNICAR assumes a fixed OC size distribution. Here, a simplified size representation is included for BrC aerosol, assuming two different size distributions for BB and BF OC based on previous studies of BrC in snow (G. Lin et al., 2014). All other OC in SNICAR is treated with the

default OC size distribution and optical properties (Hess et al., 1998).

2.3 Experimental Design

The model was run at a horizontal resolution of 0.9 ˚ latitude by 1.25 ˚ longitude with 30 vertical levels. The simulation covers 10 years from 2005 to 2014 (with one year for spin up) and has prescribed monthly sea surface temperature and sea ice concentration for the simulation period (Hurrell et al., 2008). The emissions consist of monthly BC, POA, SOA gas (SOAG), and sulfur dioxide (SO_2) emissions from CMIP6 (Feng et al., 2020), which utilizes open BB emissions from the Global Fire Emission Database version 4 with small fires (GFED4s (van der Werf et al., 2017)) and anthropogenic emissions from the Community Emissions Data System (CEDS (Hoesly et al., 2018)). Zonal (u) and meridional (v) winds are nudged to the Modern-Era Retrospective Analysis for Research and Applications, Version 2 (MERRA-2 (Gelaro et al., 2017)) reanalysis data. Three experiments were run following the aforementioned setup, all of which include BC and POA tagging. NOBRC is the control experiment with the default model configuration and includes the treatment of non-absorbing OC in snow in SNICAR. The BRC simulation includes BrC that does not undergo photochemical bleaching in the atmosphere and is treated for SDE in SNICAR. The BRC_PB simulation is the same as BRC, but includes a photochemical bleaching effect. Table 2 describes the different model runs.

Table 2: Description of the model simulations used in this study

Model Run	SimulationPeriod	Simulation type	Description
NOBRC	2005-2014	u and v winds nudged towards MERRA2 reanalysis data	Default CAM5.4
BRC	2005-2014	Same as NOBRC	CAM5.4 with th
BRC_PB	2005-2014	Same as NOBRC	Same as BRC bu

3 Model Validation

To validate our model, we compare our simulations to surface observations of in-snow BC concentration (C_{BC}; ng g^{-1}) and non-BC fraction of snow surface absorption ($f_{non\text{-}BC}$; %). The observations are from Doherty et al. (2010), X. Wang et al. (2013), and Doherty et al. (2014) that reported data from Arctic, China, and North American sample sites, respectively. Both C_{BC} and $f_{non\text{-}BC}$ are calculated from measurements of spectrally resolved absorption of snow impurities collected on a filter. By assuming an absorption Angstrom exponent (AAE) (= 450-600 nm) for BC and non-BC (or, alternatively, OC and dust separately) these studies are able to separate measured absorption into the fraction due to BC (f_{BC}) and $f_{non\text{-}BC}$. By assuming a mass absorption cross-section (MAC) for BC of 5.0-6.3 m^2g^{-1} (at = 550 nm), the f_{BC} can be used to estimate BC mass. The assumptions for MAC may bias C_{BC} high by ~20% and result in a low bias in $f_{non\text{-}BC}$, while the assumptions for AAE may introduce an uncertainty of <50% (Doherty et al., 2010). Furthermore, these observations

may exhibit significant high (C_{BC}) and low ($f_{non\text{-}BC}$) bias for samples containing high concentrations of dust particles due to instrument measurement bias (X. Wang et al., 2013).

As this work is modeling BrC SDE, it would be ideal to validate the model with observations of OC in snow. However, this data is limited by challenges in collecting soluble and insoluble OC via filtration methods and the uncertainties in post depositional processes affecting OC (Hagler et al., 2007; Xu et al., 2009). Another option is to compare the BC equivalent concentration of non-BC absorbing aerosols (BCE) (Doherty et al., 2010; Ward et al., 2018), which requires assumptions about MAC from BC, dust, and BrC, in addition to the in-snow concentrations of each. This comparison is neglected in this study given the variation in modeled BrC MAC due to emission source and photochemical bleaching (Supplementary Figure S2).

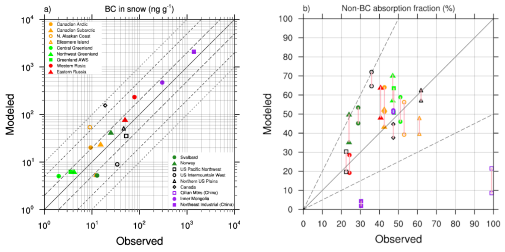

Figure 2: Comparison of snow surface variables from model and observations. (a) BC in snow concentration (ng g^{-1}) and (b) non-BC absorption fraction (%). These data are referenced in Supplementary Tables 1 and 2. The central solid line is the 1:1 line in both plots, while panel (a) shows 1:2/2:1, 1:5/5:1, and 1:10/10:1 lines (large to small dashes, respectively) and Panel (b) shows 1:2/2:1 lines (large dashes). Panel (b) shows a range in the two simulated brown carbon simulations, with photochemical bleaching (BRC_PB) and without (BRC). When BRC – BRC_PB is positive, the range is denoted with a pink line; if negative, the range is marked with a light blue line.

Figure 2 shows the comparison of C_{BC} (Fig. 2a) and $f_{non\text{-}BC}$ (Fig. 2b) from model and observations. Data is summarized in Tables S1 and S2 and the sample time and location are matched to the nearest month and latitude/longitude in

the model simulations. The model does reasonably well in reproducing the observed C_{BC} (Fig. 2a). The majority of the modeled data fall within a factor of 5 of the observations (89%), while half of the modeled data falls within a factor of 2 of the observations. The model has the greatest overestimation of C_{BC} in Southern Canada and the Northern Alaskan Coast, while it has the greatest underestimation in Svalbard, Ellesmere Island, and the Intermountain West of the US. The model tends to overestimate C_{BC} with a median model bias of +58%. Tuccella et al. (2021) conduct a similar comparison in the chemical transport model GEOS-Chem and find that their model tends to underestimate C_{BC} with a mean bias of -21%.

Figure 2b shows the $f_{non\text{-}BC}$ between BRC_PB and BRC simulations, with pink connectors signifying an increase in modeled $f_{non\text{-}BC}$ without photochemical bleaching, and light blue lines signifying a decrease. The BRC model simulation has a median positive bias of 21%, while the inclusion of photochemical bleaching (BRC_PB) has a median negative bias of -2.5%. This is a lower median bias than in the moderate absorbing BrC simulations from Tuccella et al. (2021), which tends to underestimate $f_{non\text{-}BC}$ (-17%). That being said, the BRC_PB median bias is comparable to the Tuccella et al. (2021) high absorbing BrC simulations that do not take into account photochemical aging (-3%). At nearly all of the sites, the BRC simulation has a higher $f_{non\text{-}BC}$ than BRC_PB, with the exception of the Inner Mongolia samples, which decreased by around 2%. This change is not significant given that the Inner Mongolia samples (latitude range: 40.8 ˚ N-49.55 ˚ N, longitude range: 107 ˚ E-122 ˚ E) correspond to regions of noise for the difference in BrC SDE from the two simulations (Fig. S3). The lack of consistency in SDE change between BrC and BrCPB may be explained by relatively small changes in this regions high dust deposition and/or variation in the seasonal snow cover fraction. The major outliers in Fig. 2b are the Qilan Mountains and China (Northeast Industrial), which are greatly underestimated in the model compared to observations. This may be due to a low bias in surface dust concentrations with this CESM dust scheme (M. Wu et al., 2019).

The interplay of BC and non-BC SDE can be inferred from comparisons of Fig. 2a and 2b. A few of the observations where CESM tends to overestimate C_{BC} also have an underestimation of $f_{non\text{-}BC}$ (e.g., Western Russia, Canada, China (Northeast Industrial), North Alaskan Coast). Similarly, some of the sites that underestimate C_{BC} overestimate $f_{non\text{-}BC}$ (e.g., US Intermountain West, US Pacific Northwest, Svalbard). This doesn't hold for all of the sites, however, and this is attributed to dust transport and deposition biases in the model.

4 Model Results

4.1 BC, Dust, and BrC SDE in SNICAR

Figure 3 compares the SDE from dust, BC, BrC with photochemical bleaching (BrCPB), and BrC without photochemical bleaching (Note: BrC is used to refer generically to brown carbon, but in reference to model simulations it represents brown carbon without photochemical bleaching). Combustion sectors vary for

BC and BrCPB/BrC, with Fig. 3b representing contributions from BB, BF, and FF sectors to BC SDE, while Fig. 3c,d show contributions only from BB and BF to BrCPB/BrC SDE. The BrCPB/BrC SDE are calculated by taking the difference in OC SDE from the BRC/BRC_PB simulations and the NOBRC simulation. This neglects contributions from SOA and FF POA, which are not treated as BrC. The global BC SDE (0.057 Wm^{-2}) is similar to SDE calculated in Flanner et al. (2007) of 0.041-0.044 Wm^{-2} (only for the land contribution). Here BC SDE is larger compared to dust (0.014 Wm^{-2}) and BrCPB (0.021 Wm^{-2}), and contributes more to SDE in South Eastern Asia due to FF BC deposition. However, global average BrC SDE (0.056 Wm^{-2}) is comparable to BC. The inclusion of other non-BrC sources for OC (FF POM and SOA) increases the OC global mean SDE to 0.032 and 0.067 Wm^{-2} for bleaching and non-bleaching simulations, respectively, making OC SDE without bleaching effect larger than the all sources of BC combined. The global BrC SDE appears to be driven by larger BrC contributions to Siberian and Antarctic SDE. For both BC and BrC, the main global regions where SDE is the largest are the Arctic, the Tibetan Plateau (TP), and Antarctica, with maximum BrC and BC SDE of around 1 Wm^{-2}.

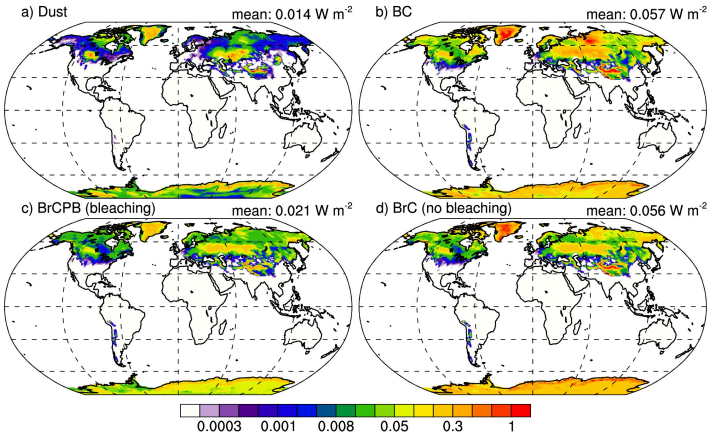

Figure 3: Modeled snow darkening effect (SDE) from different light absorbing particles. Contributions to total SDE (Wm^{-2}) calculated in SNICAR from the three absorbing species: a) dust, b) black carbon (BC), and c, d) brown carbon (BrC), with and without atmospheric photochemical bleaching, respec-

tively. The BC SDE includes all source contributions (i.e., fossil fuel, biofuel, and biomass burning), while BrC only includes biomass burning and biofuel contributions to SDE. The SDE is averaged over all grid areas, with and without snow cover. Numbers at the upper-right corner of each panel are the corresponding global mean SDE.

The ratio of globally averaged BrC-to-BC SDE is 37% and 98% for BrCPB and BrC, respectively. This is a larger contribution to global SDE from BrC than G. Lin et al. (2014) (24% that of BC) or Tuccella et al. (2021) (15%-30% that of BC), corresponding to BrC SDEs of 0.021-0.056 Wm^{-2} (our model), 0.0066 Wm^{-2} (Tuccella et al., 2021), and 0.0020–0.0055 Wm^{-2} (G. Lin et al., 2014). One possible explanation for these differences is the different aerosol deposition of BC and OC, where high-latitude BC deposition tends to be lower in the G. Lin et al. (2014) simulations compared to simulations from Flanner et al. (2007, 2009), the latter of which both use CAM3 and CLM3. Another possible explanation is a difference in snow cover between the two models, where offline snow cover fraction is lower in G. Lin et al. (2014) over Asia than in coupled atmosphere-land simulations in Flanner et al. (2007, 2009). Lastly, the use of different snow albedo parameterizations – Dang et al. (2015) in Tuccella et al. (2021) versus SNICAR in this study – may explain our larger SDE due to processes unique to SNICAR such as the collection of absorbing aerosols at the surface of snowpack and feedbacks on snow grain size and snow cover fraction. Assumptions regarding BrC MAC don't seem to explain these model differences given that the BrC MAC in our simulations tends to be lower than BrC MAC in Tuccella et al. (2021) (Figure S2).

4.2 Regional Impacts of BB+BF BrC

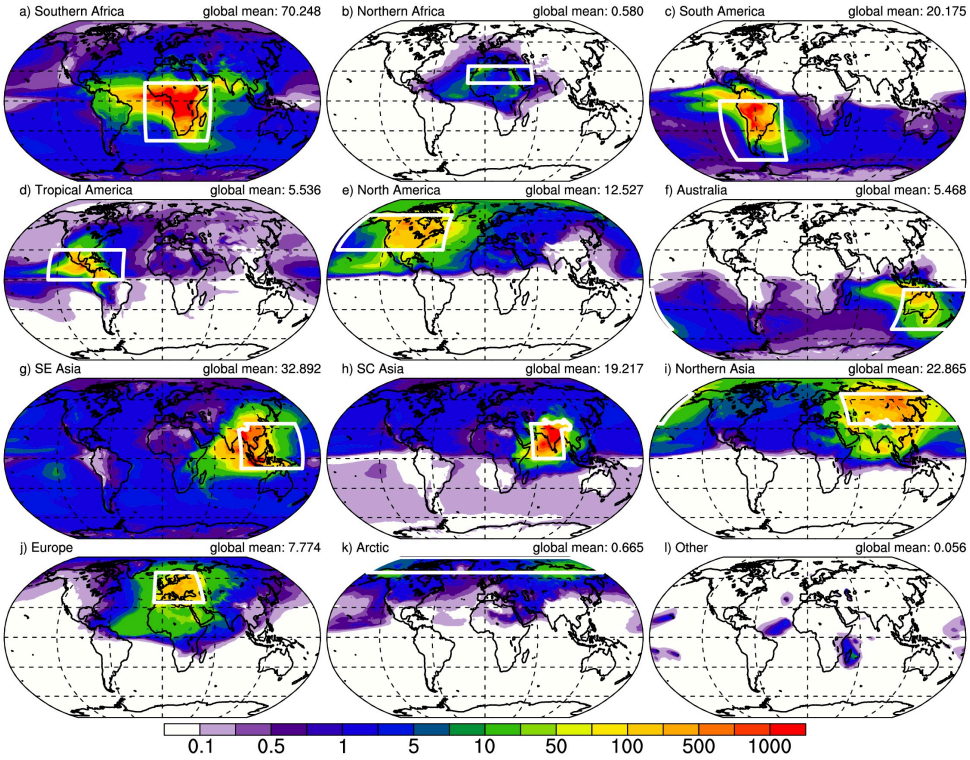

Figure 4: Regional contributions to the 10-year mean POA deposition flux (µg m^{-2} day^{-1}) from BB and BF sources. Deposition is from the BRC simulation and the regions in each panel are described in Fig. 1.

The tagging method applied to carbonaceous aerosol allows us to assess aerosol transport and contributions to SDE from the 12 different source regions. Figure 4 shows the deposition flux (µg m^{-2} day^{-1}) of BB and BF POA (i.e., sources of BrC in our model) from each region defined in Fig. 1. By far the largest contributor to global deposition flux is Southern Africa (SAfr) (Fig. 4a) followed by Southeast Asia (SEAs) (Fig. 4g), Northern Asia (NAs) (Fig, 4i), South America (SAm) (Fig. 4c), and South Central Asia (SCAs) (Fig. 4h). Generally speaking, northern hemisphere (NH) emissions from North Africa (NAfr), North America (NAm), NAs, Europe (Eur), and the Arctic (Arc) remain in the NH, and southern hemisphere (SH) emissions from Aus and SAm remain in the SH. Emission sources nearer the equator (i.e., SAfr, Tropical America (Tam), SCAs,

and SEAs) can be transported to both NH and SH. With sources of aerosol in the SH at lower latitudes, the maximum SDE in Antarctica is expected to be lower than that in the Arctic (as shown in Fig. 3). However, more than half of the global BB aerosol are emitted from SAfr, SAm, and Aus (van der Werf et al., 2017), indicating that strong burning seasons could have a large impact on Antarctic SDE. In regard to the emissions near the equator, the mechanism for the transport of these emissions is driven by deep convection in the intertropical convergence zone (ITCZ), which transports aerosol to the upper atmosphere and allows for more efficient global distribution of BrC.

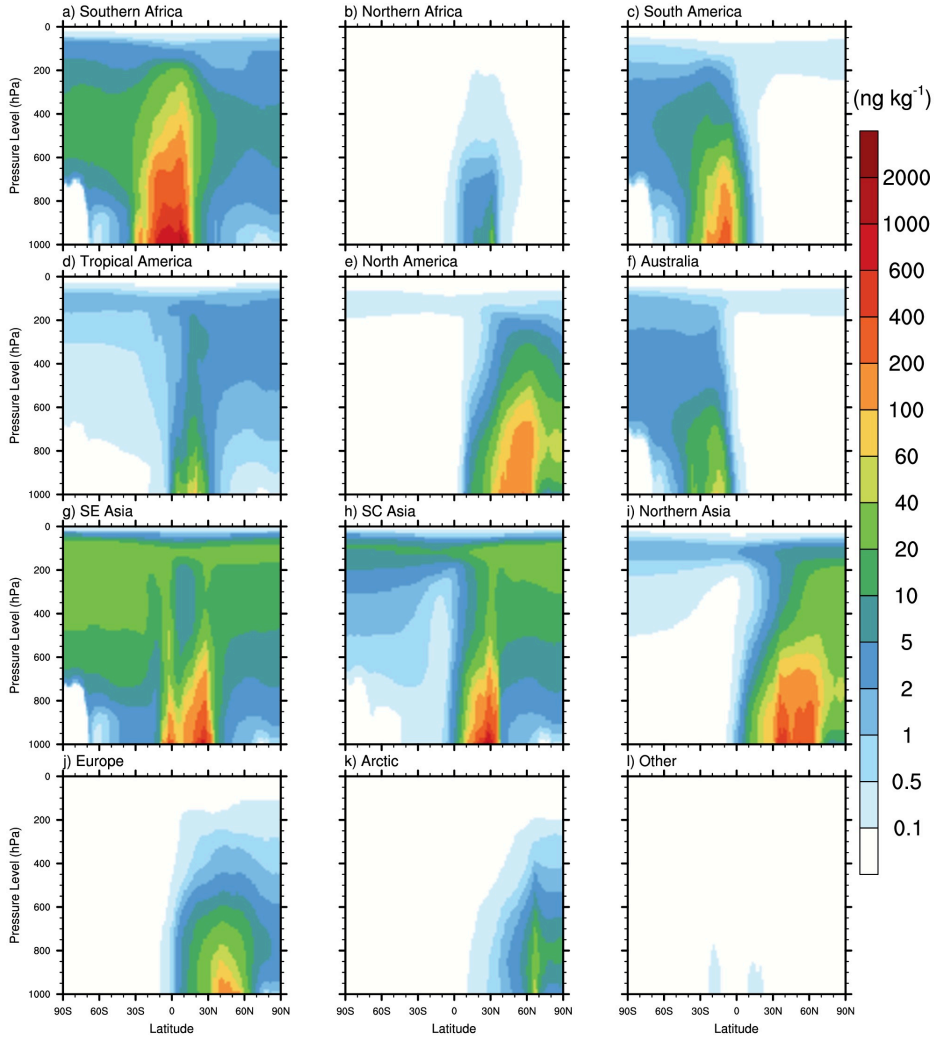

Figure 5: Regional contribution to the 10-year, zonal mean vertical cross section of POA mixing ratio (ng kg^{-1}) from BB and BF sources. The POA mixing

ratio is from the BRC simulation, and the regions are described in Fig. 1.

The effects of deep convection on the regional emissions are clear in Fig. 5, which shows the zonal mean vertical cross-section of BB and BF POA mixing ratio (ng kg^{-1}) from each of the tagged source regions. As indicated in Fig. 4, emission sources near the equator undergo strong vertical transport, resulting in the upper-level transport to both poles. The greatest vertical transport occurs in SEAs (Fig. 5g) and SCAs (Fig. 5h). In SEAs, the peak centered on ~0 ° latitude is due to BB emissions from Indonesia.

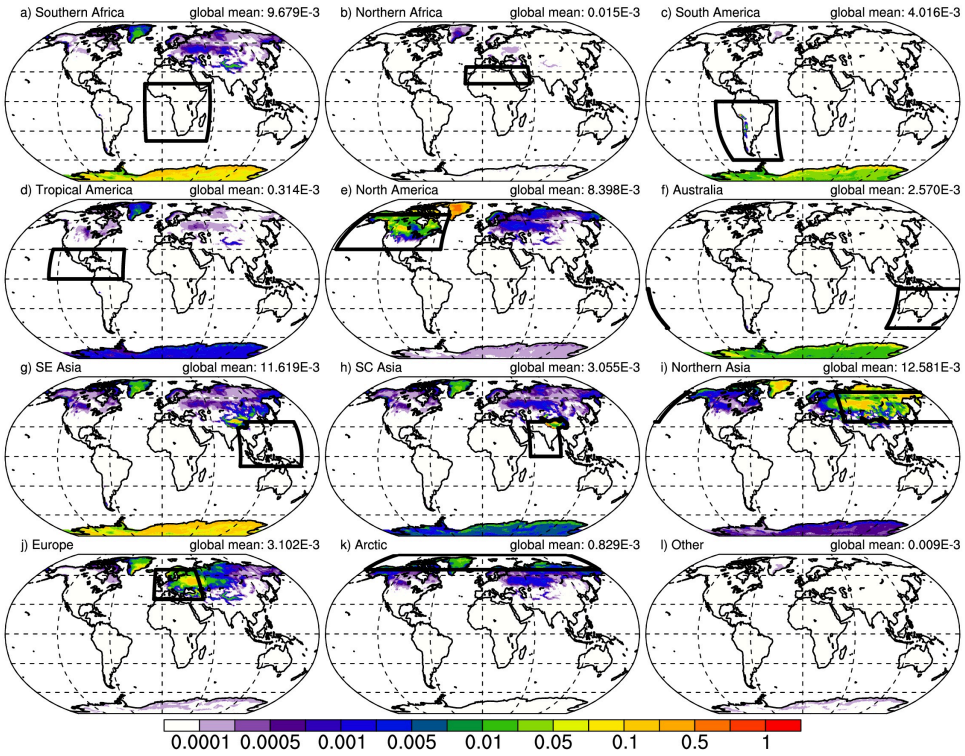

Figure 6: Regional contribution to the 10-year mean BrC snow darkening effect (SDE; Wm^{-2}) from BB and BF sources. The SDE is from the BRC simulation (non-bleaching BrC) so it represents the upper bound for BrC contribution to SDE. Emission regions are marked in each panel with a solid black box and correspond to the regions in Fig. 1. The BrC SDE is averaged over all grid areas, with and without snow cover.

The total BrC SDE from Fig. 3 can be separated into regional contributions by weighting SDE by regional deposition flux (Fig. 4), as shown in Fig. 6. The BrC SDE from hydrophobic and hydrophilic OC is weighted separately and summed to take into account the different meltwater scavenging fractions for each of these bulk OC species. The major regional contributors to global BrC SDE do not necessarily correspond to the regions with highest deposition flux in Fig. 4. The proximity of NAs BB and BF emission sources to land snow and ice lead to the largest contribution to BrC SDE, 0.0126 – which is 0.0064 Wm^2 if the bleaching effect is considered (BrCPB; Fig. S4i) – concentrated over Asia, Greenland, and Alaska. The second largest contribution to global SDE is from SEAs (0.0116/0.0034 Wm^{-2}; Fig. 6g/Fig. S4g), with the greatest SDE over the Tibetan Plateau, Antarctica, and Greenland. The global mean SEAs SDE from BrCPB is 29% that of BrC, while the global mean NAs BrCPB SDE is 51% that of BrC. This is telling of more effective bleaching of BrC from SEAs after emission and during transport to snow covered regions. Emissions from NAm (0.0084/0.0033 Wm^{-2}; Fig. 6e/S4e) and SAfr (0.0097/0.0027 Wm^{-2}; Fig. 6a/S4a) are the next largest contributors to global BrC SDE. Similar to SEAs, SAfr BrC is more impacted by photochemical bleaching leading to a BrCPB SDE that is 28% that of BrC, compared to a NAm BrCPB SDE that is 39% that of BrC. The BrC (BrCPB) SDE regional contributions from NAs, SEAs, SAfr, and NAm account for 23% (31%), 21% (16%), 17% (13%), and 15% (16%) to the global BrC (BrCPB) SDE, respectively.

Figure 6 emphasizes that the distance of emission sources to snow and ice covered surfaces plays a large role in deposition and resulting SDE. This is true of NAm, Eur, and NAs impacts in the Arctic. It is also exemplified by the SEAs (Fig. 6g) and SCAs (Fig. 6h) regions, which contribute the most to BrC SDE over the TP. This is also an important consideration for the BrC treatment because the reduced aerosol transport may lead to less photochemical bleaching. As a result, the BrC that is deposited in the regions close to sources may be more absorbing than in distant regions.

4.3 Carbonaceous Aerosol Contributions to SDE in Major Receptor Regions

To understand the relative effects of BC and BrC on high-impact SDE zones, this study isolates 4 regions of focus: the Arctic (60 °N–90 °N), the Antarctic (60 °S–90 °S), the Tibetan Plateau (TP; 25 °N–45 °N, 60 °E–110 °E), and the Rocky Mountains of the United States (RM; 37 °N–49 °N, 242 °E–258 °E) (Fig. 7). The RM and TP regions are roughly based on previous modeling studies of SDE in these regions (Rahimi et al. (2020) and Rahimi et al. (2019), respectively). Of these regions, the greatest contributions to the global SDE from BrC come from the Arctic (26.8% (BRC), 26.5% (BRC_PB)) and the Antarctic (48.7% (BRC), 35.5% (BRC_PB)).

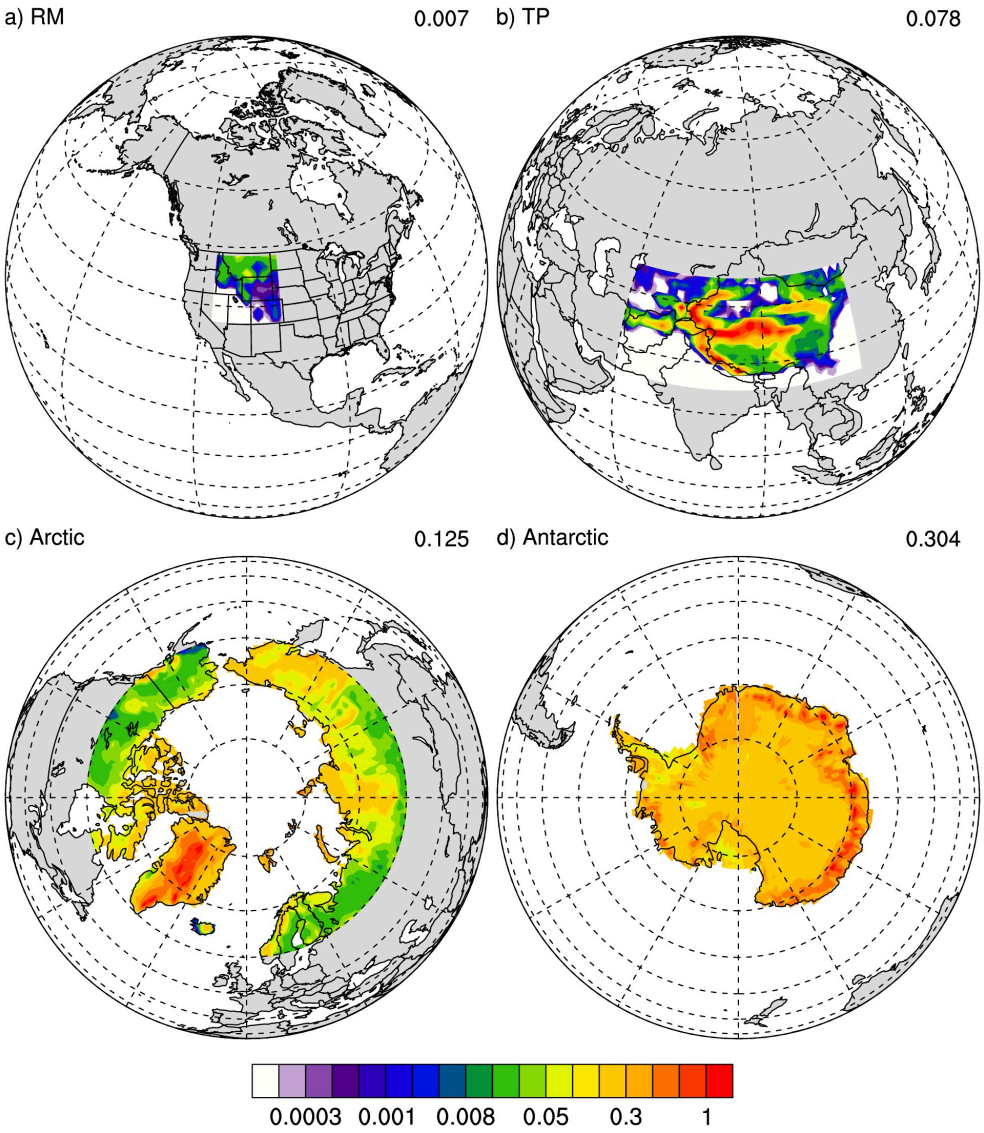

Figure 7: Regional BrC SDE. 10-year mean BrC SDE (Wm^{-2}) without photochemical bleaching (BRC simulation) from all BB and BF sources over a) the Rocky Mountains (RM), b) the Tibetan Plateau (TP), c) the Arctic, and d) the Antarctic that act as major contributors to global snow darkening effect. The SDE is averaged over all grid areas in the region, with and without snow cover.

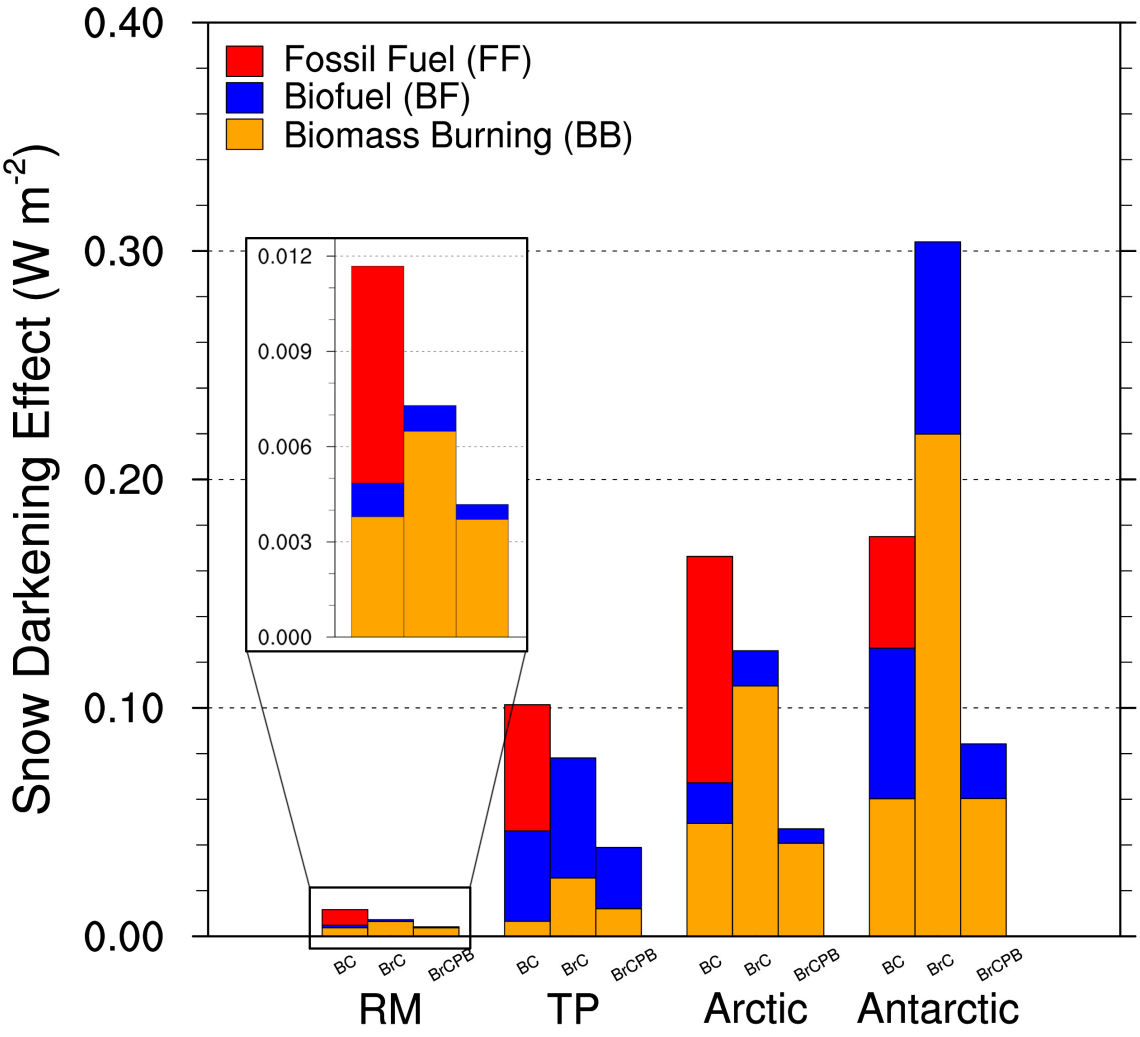

Figure 8: Fuel sector contributions to regional SDE. Total contributions from BC and OC to the 10-year mean SDE over the four regions: Rocky Mountains (RM), Tibetan Plateau (TP), the Arctic, and the Antarctic. These contributions are broken down into their sector contributions: fossil fuels (red), biofuel (blue), and biomass burning (orange). Contributions from BrC are from both simulations, with (BrC) and without photochemical bleaching (BrCPB); BC is from the BRC simulation. The SDE is averaged over all grid areas in the region, with and without snow cover.

The fuel sector deposition-fluxes for BC and BrC are used to isolate the contributions to SDE from these carbonaceous species in each of these regions (Fig. 8). The fuel sectors are represented by orange (BB), blue (BF), red (FF), and teal (OC from FF and SOA deposition). The BrC and BrCPB SDE is plotted from the BRC and BRC_PB simulations, respectively. The BC SDE is from the BRC simulation. Figure 8 shows that BC SDE from all sources is the most prevalent forcing agent in most of these zones. The BC SDE is mostly due to BF and FF sectors, with larger fractional contributions from BB in the Arctic and Antarctic. In the TP, Arctic, and Antarctic the BrCPB SDE (0.039, 0.047, and 0.084 Wm^{-2}) is comparable to BC SDE from BB and BF (0.046, 0.067, and 0.126 Wm^{-2}) (Table 3). However, the removal of the bleaching effect leads to a BrC SDE that is much larger than BC SDE from these same sources (0.078, 0.125, and 0.304 Wm^{-2}) (Table 3). The Arctic and Antarctic BC SDE is comparable, with the former driven more by FF/BB and the latter driven more by BF/BB (though FF also contributes significantly to the Antarctic SDE). Surprisingly, BrCPB (BrC) SDE is the greatest in Antarctica, supplementing approximately half (twice) the regional SDE of BC from all sources. Assuming that the actual BrC SDE lies somewhere between BrC and BrCPB, BrC may be the largest contributor to Antarctic SDE which is itself the largest regional contributor to global SDE. Also, this global contribution could be expected to be even larger than shown here given the lack of BrC SDE over sea ice in our model.

Table 3: Regional and global mean SDE (mWm^{-2}) for BC, BrC, BrC with photochemical bleaching (BrCPB), and non-BrC sources for the fuel sectors described in Fig. 9. Included are ±1 standard deviation. All BC values are calculated from the BRC simulation

	Rocky Mountain	**Tibetan Plateau**	**Arctic**	**Antarctic**	**Global**
BC					
BB	3.8±0.2	6.6±0.6	49.4±17.6	60.2±18.9	10.7±3.2
BF	1.1±1.5	39.5±7.8	17.8±6.3	65.9±8.7	13.9±1.2
FF	6.8±8.9	55.2±12.3	99.1±17.3	49.0±7.1	32.6±2.4
Total	**11.7±10.6**	**101.3±24.6**	**166.3±37.6**	**175.1±24.6**	**57.3±5.3**
BrC					
BB	6.5±0.8	25.6±3.0	109.6±32.3	220.0±82.4	34.5±7.4
BF	0.8±5.9	52.5±11.6	15.4±3.0	84.1±13.6	21.7±2.4
Total	**7.3±6.6**	**78.1±13.6**	**125.0±32.2**	**304.1±78.0**	**56.2±7.0**
BrCPB					
BB	3.7±0.4	12.1±1.2	40.8±11.9	60.3±0.0024	11.±2.4
BF	0.5±3.2	26.8±5.2	6.3±1.1	23.9±0.004	10.4±1.1
Total	**4.2±3.6**	**38.9±5.9**	**47.1±11.6**	**84.2±0.0228**	**21.4 ±2.3**
Non-BrC					
Total	**0.4±0.9**	**0.4±3.0**	**40.3±3.5**	**69.0±7.4**	**11.1±0.7**

The non-BrC OC (i.e., the OC SDE from the NOBRC simulation) has significant

contributions to SDE over the Arctic and Antarctic, but has very little impact on SDE over RM and TP (Table 3; Fig. S5). This is due to the presence of high deposition rates of BC and dust in the RM and TP regions which darkens the underlying snow and corresponds to negative forcing for the weakly absorbing non-BrC (Figs. S6 and S7).

4.4 BB+BF Source Contributions to SDE in Major Receptor Regions

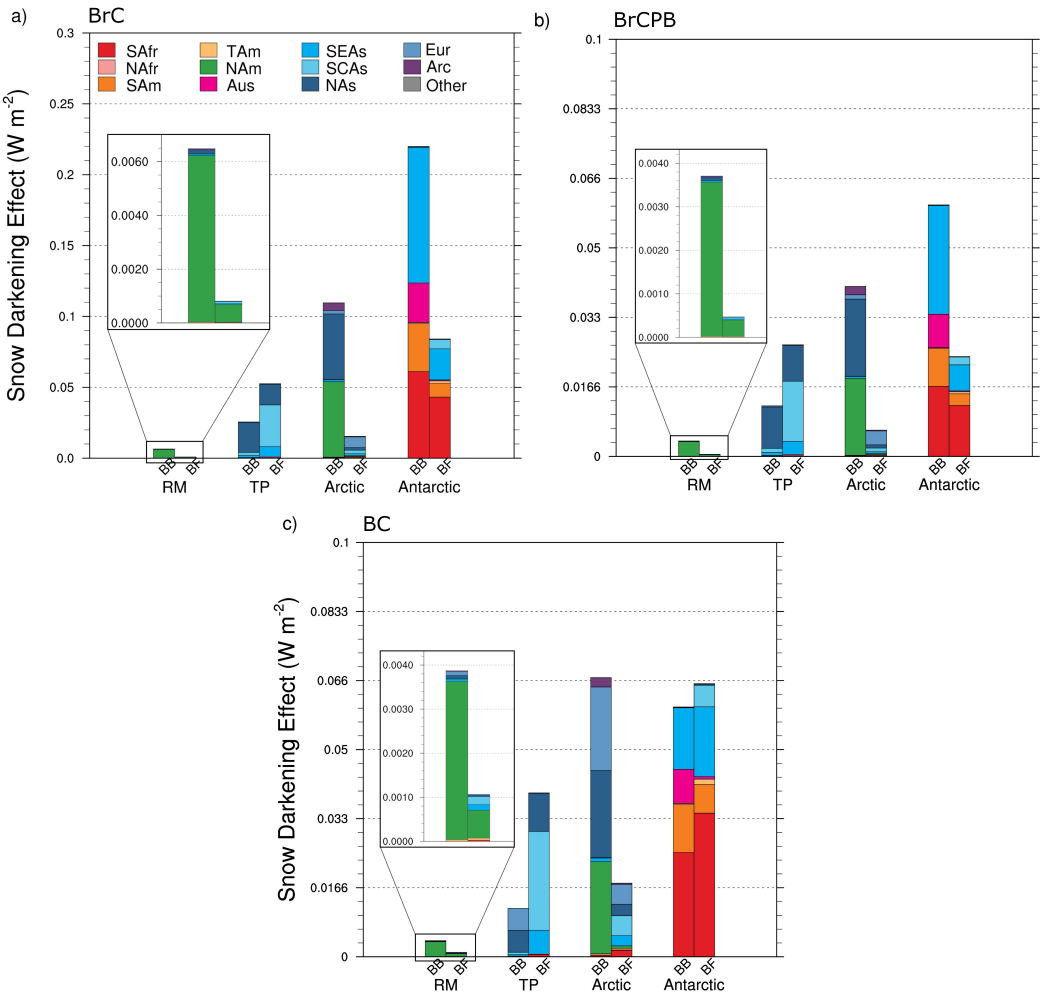

Figure 9: Source contributions to regional SDE. Contributions from biomass burning (BB) and biofuel (BF) sources of (a) BrC, (b) BrCPB, and (c) BC to the 10-year mean SDE over the four regions detailed in Fig. 7: Rocky Mountains,

Tibetan Plateau, the Arctic, and the Antarctic. Source regions are specified in Fig. 1. The SDE is averaged over all grid areas in the region, with and without snow cover.

Figure 9 further separates the BB and BF source contributions to SDE into fractional contribution from the tagged emission sources described in Fig. 1. The sources are separated into BrC (Fig. 9a), BrCPB (Fig. 9b), and BC (Fig. 9c). Note that the range of y-axis values differs between panel a and panels b and c.

Most of these region's SDE is driven by close-proximity sources. Over the RM receptor region, BrC SDE is driven by local emissions from NAm BB and BF. A 2% contribution to RM BB SDE also comes from NAs, though the overall effect on SDE is small due to weak contribution to global SDE from RM. The TP BrC SDE is mostly attributed to BF emissions from SCAs, NAs, and SEAs, and about one third the TP BrC SDE is associated with BB emissions from NAs. The majority of Arctic BrC SDE is associated with BB emissions from NAm, NAs, and to a lesser extent, Arc. BF emissions are a smaller contributor to Arctic BrC SDE (14%) and are mainly from Eur. The Antarctic has the most diverse set of aerosol sources of the four regions detailed here. As might be expected, most of the sources are from the SH, but a large fraction of BB and BF emissions also come from SCAs and SEAs. Just under half of the BB BrC SDE in Antarctica can be attributed to SEAs emissions from Indonesian BB, while the rest comes from SAfr, SAm, and Aus. Emissions from BF sources in SAfr and SAm drive BrC BF SDE, but significant contributions are also associated with SCAs, SEAS, and TAm sources. Inclusion of the photochemical bleaching effect (BrCPB; Fig. 9b) does little to change the relative source contributions to SDE. However, the magnitudes of the BB and BF BrCPB SDE in RM, TP, Arctic, and Antarctic are reduced to 57%, 50%, 38%, and 28% the forcing of BrC, respectively.

The BC SDE in the four receptor regions (Fig. 9c) has slightly different source and sector contributions to SDE than BrC. Larger relative contributions from BF than BB for BC compared to BrC/BrCPB can be partly explained by the higher BC/OC emission ratios from this sector. Over RM, the BC SDE follows a similar source region makeup as BrC but with more of an influence from SEAs/SCAs BF. In TP, there is a larger contribution from SCAs BF BC than for BrC. Also, the BB BC SDE in TP consists more of BB emissions from Eur than BrC. Similar to TP, the Arctic has larger Eur contribution to BB BC SDE. This can be explained by ~88% of emissions from GFED consisting of Savannah and Agriculture categories with higher BC/OC emission ratios (van der Werf et al., 2017), which have a greater impact on BC SDE than BrC SDE in the model. The Arctic SDE has various BC BF sources from the NH, but is also affected by long-range transport from SCAs, SEAs, and SAfr. Lastly, Antarctica is the only region that has a SDE that is driven by BF BC aerosol deposition. The BB BC SDE has a larger contribution from SAfr than BrC SDE due to higher BC/OC emission ratios from SAfr in GFED. Emissions of BC from the SAfr

region also drive BF BC SDE followed by SEAs, SAm, and SCAs.

4.5 Seasonal Variation in SDE over Major Receptor Regions

Another important factor in understanding the global climate impact of BrC SDE is the seasonality of BrC in the four receptor regions. Figure 10a shows the monthly average BrC/BrCPB SDE (solid line/dashed line), color-coded by the four receptor regions: RM (orange), TP (purple), Arctic (green), and Antarctic (maroon). The shaded range in SDE represents ±1 standard deviation about the 10-yr monthly mean.

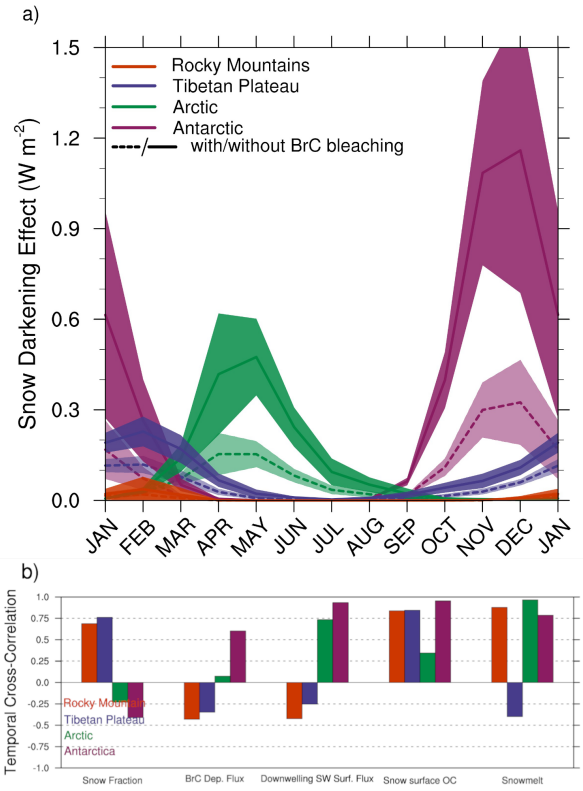

Figure 10: Seasonal variation in regional BrC SDE and correlation with variables affecting SDE calculations. a) Variation of 10-year monthly mean (± one standard deviation) BrC and BrCPB SDE from the four regions described in Fig. 8, and b) temporal cross-correlation between monthly mean BrC SDE and variables that play into the calculation of SDE, including snow fraction (%),

BrC deposition flux (kg m^{-2} s^{-1}), downwelling shortwave surface flux (Wm^{-2}), snow surface layer OC (kg m^{-2}), snowmelt (mm s^{-1}). Colors represent the Rocky Mountains (orange), the Tibetan Plateau (purple), the Arctic (green), and the Antarctic (maroon). The dashed line in Panel a denotes BrCPB. The SDE is averaged over all grid areas in the region, with and without snow cover.

The monthly variation in BrC SDE in the four regions shows that global SDE has three main forcing modes: February (RM/TP), May (Arctic), and December (Antarctic) (BC+dust SDE in our model has a similar multi-modal pattern (Fig. S8)). The largest maximum monthly SDE due to BrC/BrCPB is in Antarctica (1.16/0.32 Wm^{-2}), followed by the Arctic (0.48/0.15 Wm^{-2}), TP (0.23/0.12 Wm^{-2}), and RM (0.04/0.02 Wm^{-2}). Having a seasonality in SDE – both for BrC and BC+dust – indicates that regional impacts on meltwater runoff and climate forcing differ greatly about the globe and can sustain a 10-month period when SDE contributes significantly to regional climate forcing. The range in seasonal maxima in the different regions indicates a complex interplay of local conditions that include, but are not limited to, surface insolation, snow cover fraction, and in-snow LAPs.

The role of SDE factors at the four receptor regions is explored in Fig. 10b, which shows the temporal cross-correlation (TCC) of five mechanisms accounted for in calculations of SDE in SNICAR (see Eq. S1). These include snow-cover fraction (%), BrC deposition flux (kg m^{-2} s^{-1}), downwelling shortwave (SW) surface flux (Wm^{-2}), snow surface layer OC (kg m^{-2}), and snowmelt (mm s^{-1}). The variables snowmelt, snow cover fraction, and surface OC are impacted by feedbacks from BrC SDE. The TCC is used to compare the offset, or lag, in the seasonal cycling of these variables, where a coefficient of 1.0 indicates that the cycles are correlated (i.e., no offset in the cycles), a coefficient of -1.0 indicates that cycles are anti-correlated (i.e., offset by radians), and a coefficient of 0 means the cycles are offset by /2 radians. Due to the similarities between BrC and BrCPB, TCC are only calculated for BrC.

The lower latitude regions, RM and TP, have similar behavior in Fig. 10b. Snow conditions in RM may favor the accumulation of insoluble OC aerosol on the surface of the snowpack as well as large effective snow radius changes with melting snow given that its BrC/BrCPB SDE is strongly correlated with surface OC concentrations (0.84) and snowmelt (0.88), respectively. This region also has a BrC SDE that is correlated with snow-cover fraction (0.69), indicating the importance of the seasonal snow cover in this region for SDE. Seasonal snow cover also drives a weak anti-correlation of RM BrC SDE with the direct deposition flux of BB and BF BrC (-0.43) and the surface insolation (-0.42), due to there being no snow in the peak months for BrC deposition (August) and surface insolation (June). The TP has a similar correlation to snow-cover fraction (0.76) and snow surface OC (0.85) as RM, as well as a similar anti-correlation to BB and BF BrC deposition flux (-0.35) and surface insolation (-0.25). A slight negative correlation with snowmelt (-0.4) may be indicative of a larger spread in peak snowmelt over TP, where snowmelt decreases during

the peak rainfall season of June to August (Krishnan et al., 2016) but increases again in September through November (Fig. S9). In addition to being strongly correlated with surface OC concentrations, both RM and TP BrC SDE have a strong correlation with integrated column OC concentrations (0.98 and 0.99, respectively) (Fig. S10). This indicates the importance of hydrophobic aerosol retention within the snowpack and on the snow surfaces of these two regions.

The Arctic and Antarctic regions both differ from RM and TP in a persistence of larger snow cover fractions throughout the entire year (Fig. S10). Based on Fig. 10b snow cover appears to be less of a limiting factor at the poles with a nearly uncorrelated BrC SDE with snow cover fraction in the Arctic (-0.23), while in the Antarctic there is a slight anti-correlation (-0.41). Where these two regions show higher TCC is in the correlation of BrC SDE with surface SW insolation (Arctic: 0.73, Antarctic: 0.95) and snowmelt (Arctic: 0.97, Antarctic: 0.79). The Arctic BrC SDE maximum agrees well with previous reporting of peak incident solar radiation on land-ice (Flanner et al., 2009). Based on these TCC, the feedbacks on snow albedo with snowmelt appear to play a larger role in the Arctic BrC SDE while peak solar flux correlates better with Antarctic BrC SDE. This may be due to the Antarctic snow surface being centered about 90 $^\circ$ S, while the Arctic land snow surface is spread over slightly lower latitudes. The Antarctic also has a uniquely high correlation with BB and BF BrC deposition (0.6) compared to other regions. This correlation is driven by BB BrC deposition (Fig. S10), with peak deposition in October (Fig. S11). The BrC deposition over Antarctica is much lower than other regions, but BrC SDE and surface OC have a strong TCC (0.95). This may indicate the importance of hydrophobic OC retention in snowpack and concentration at the surface for BrC SDE in Antarctica.

What this comparison illuminates is the importance of different physical mechanisms for the calculated BrC SDE in the four receptor regions detailed here. How snow cover fraction is modeled can have a large impact on modeled SDE in lower latitude regions (e.g., RM, TP). Furthermore, representing feedbacks in snow albedo due to snow grain-size evolution and aerosol melt-water scavenging could have large impacts for aerosol SDE maxima across the globe (e.g., Qian et al., 2014).

5 Discussion and Conclusions

The implementation of BrC deposition on snow has only been included in a few modeling studies with a variety of assumptions made to take into account the evolving understanding of this atmospheric process. These assumptions include constant BrC RI for primary and secondary sources (Jacobson, 2012; Yasunari et al., 2014) or a range of BrC RI to take into account the variation due to source region burning conditions and photochemical bleaching (G. Lin et al., 2014; Tuccella et al., 2021). Our work differs from these previous studies in its treatment of primary BrC absorption as temporally and spatially varied, dependent on emission source and photochemical bleaching. The photochemical bleaching effect is stronger near the equator than at the poles (due to higher [OH]

in the tropics) while the emission of BrC from sources with higher BC-to-POA ratio (e.g., BF, BB from savannah and grass fires) tends to be more absorbing. This leads to a complex interplay of source and transport that contributes to a range of BrC imaginary RI over different snow surfaces across the globe.

When compared to observations (Fig. 2), this work shows an improvement in CESM of $f_{non\text{-}BC}$ when BrC photochemical bleaching is included (median model bias of -2.5%). Outliers in this comparison are attributed to dust biases in CAM. This BRC_PB simulation is closer to observations than Tuccella et al. (2021), which reported a median model bias of -17%. The BRC_PB simulation is more similar to the high absorbing test of (Tuccella et al., 2021) (median model bias -3.0%) that assumes no photochemical bleaching.

Our model simulates a global BrC/BrCPB SDE that is comparable to BC SDE and is higher than that calculated in other studies (Fig. 3). The ratio of globally averaged BrC-to-BC SDE ranges from 37% to 98% between simulations with and without photochemical bleaching, respectively. This is larger than other estimates of BrC SDE, which range from 15-30% BC SDE (G. Lin et al., 2014; Tuccella et al., 2021). This could be partly explained by differences in snow cover fraction and aerosol deposition between the different host models (G. Lin et al., 2014). Also, the aerosol feedbacks on snow cover fraction and snow grain size treated in SNICAR may lead to larger SDE than in Tuccella et al. (2021), which uses a snow albedo parameterization without these physical mechanisms.

Regional tagging identifies the four major source regions of BrC deposition in our model as SAfr, SEAs, NAs, and SAm (Fig. 4). Emission sources near the equator allow for transport of BrC into both the SH and the NH. This is especially true of SEAs, where BB emissions from Indonesia are lifted into the upper atmosphere and transported poleward (Fig. 5). When regional deposition flux is used to weight BrC SDE, a different hierarchy emerges for regional contributions to SDE (Fig. 6, S4). The tagged NAs region contributes the most to global BrC (BrCPB) SDE (23% (31%)) followed by SEAs (21% (16%)) and SAfr (17% (13%)). The SAm region plays a smaller role in SDE than it does in global BrC deposition and is superseded by NAm (15% (16%)) as the fourth largest contributor to global BrC (BrCPB) SDE. The impact of each tagged region on SDE depends on its proximity to land snow and ice surfaces given the larger global contributions to SDE from NAs and NAm. Transport from equatorial emission sources such as SAfr and SEAs is an exception to this rule. Photochemical bleaching also impacts SDE, where long-range transport and equatorial emissions undergo stronger photochemical bleaching. Going from BrC to BrCPB, there is a reduction of regional global fraction of SDE in SAfr, SEAs, and SAm and, conversely, an increase in regional global fraction of SDE in NAs and NAm. This describes a weaker bleaching in NAs and NAm (i.e., less of a difference in BrC versus BrCPB SDE), and a stronger bleaching in equatorial emissions (i.e., more difference in BrC versus BrCPB SDE).

While the previous findings describe the relative contributions from emission sources to global SDE, this study also addresses the attribution of tagged emis-

sions of BC and BrC to specific SDE receptor regions. The RM, TP, Arctic, and Antarctic regions (Fig. 7) are chosen for their contributions to global climate impacts of SDE, both due to their proximity to population centers (e.g., RM, TP, Arctic) and their majority share of the Earth's cryosphere (e.g., Arctic, Antarctic). Of these four zones, the Arctic and Antarctic are the largest contributors to global SDE (Fig. 8), in large part due to their expansive snow surface area. The BC SDE from all sources tends to be the most prevalent forcing agent. BrCPB SDE is comparable to BC SDE from the same sources, and the removal of photochemical bleaching leads to a BrC SDE that is consistently larger than BB+BF BC SDE. This is especially true in the Antarctic, which is already estimated as the largest regional contributor to global SDE in CESM. This suggests that BrC may have a larger impact on Antarctic SDE than has been shown previously. That being said, there is uncertainty in this finding given the lack of land-based observational data from Antarctica.

Further isolating the BB and BF sectors in the receptor regions into their emission regions (Fig. 9) reinforces the importance of proximity of emission to SDE. This is especially true of the RM and TP regions, which are influenced by NAm and SCAs/NAs/SEAs sources, respectively. The SDE in polar regions – Arctic and Antarctic – is mainly affected by the corresponding hemispheric sources. The exceptions to this rule are mainly in Antarctica, where transport from equatorial emission sources in SEAs, SCAs, and TAm contributes significantly to SDE. Proximity of source also contributes to photochemical bleaching impacts, where the ratio of BrCPB to BrC in RM, TP, Arctic, and Antarctic is 57%, 50%, 38%, and 28%, respectively. Lastly, in Fig. 9 the comparison of BC and BrC/BrCPB highlights the larger impact on BC SDE from sources with larger BC-to-POA emission ratios. These emission sources include BF emission sources and Eur and SAfr BB emissions. This is seen in the larger relative contribution to SDE from BC BF emissions, larger contributions from Eur BB BC to SDE in the Arctic and TP, and greater contributions from SAfr BB BC to SDE in Antarctica and the Arctic.

Seasonal variation in BrC/BrCPB SDE over the four receptor regions exhibits a span in regional peak SDE, supplying a near-annual input to global SDE (Fig. 10a). The range in regional modes in SDE reflects an interaction of the environmental factors that affect SDE calculations. These range from processes external to SDE such as surface insolation and BrC deposition, to factors like surface OC concentrations, snow cover fraction, and snow melt that are tied to BrC SDE. In RM and TP, BrC SDE has a high TCC with snowmelt and surface concentrations of OC, indicating the importance of hydrophobic retention, aerosol scavenging, and snow grain evolution in these regions. Snow cover fraction is also correlated with BrC SDE in RM and TP, demonstrating how the seasonality of snow cover limits the extent of SDE. In the Arctic and Antarctic, where snow and land ice are present year-round, BrC SDE has a better correlation with insolation and snowmelt. This year-round snow cover is most evident in Antarctica (Fig. S11), which results in a high correlation between SDE and BB deposition flux (Fig. S12). Peak deposition over Antarctica (0.12

ng m^{-2} s^{-1}) is almost two orders of magnitude smaller than the other regions (RM: 9.93 ng m^{-2} s^{-1}, TP: 4.72 ng m^{-2} s^{-1}, Arctic: 6.13 ng m^{-2} s^{-1}). However, BrC SDE is strongly correlated with snow surface and in-column OC suggesting that the Antarctic BrC SDE is a result of OC accumulation in the snowpack. All of the regions here exhibit some sort of dependence on modeled snow, such as snowmelt, snow cover, or aerosol accumulation in the snowpack. As a result, the representation of the feedbacks between aerosol and snow in the model may have a large impact on the seasonality of BrC, BC, and dust SDE calculations in models.

The estimations of BrC and BC SDE in this work are likely biased low due to assumptions made in designing these experiments. First, our version of SNICAR neglects SDE over sea ice. Including sea-ice would increase the surface area that could be darkened by absorbing aerosols, increasing the regional contribution to global SDE. In the Arctic and Antarctic, including sea ice would increase the snow and ice surface area of these regions by 64% and 74%, respectively (Table S3, Fig. S13). In this study, the model also neglects embedded BC and BrC in snow grains, the former of which can increase SDE 43%-86% compared to treating BC as externally mixed in the snowpack (Flanner et al., 2012; He et al., 2018b; H. Wang et al., 2020). Lastly, incorporating a more detailed secondary BrC formation mechanism might also increase BrC SDE, as NO_x-driven absorption enhancement (Li et al., 2020; P. Lin et al., 2017; Zhong & Jang, 2014) might contribute to a stronger absorbing SOA than treated here.

With increasing BB activity in both North America (Abatzoglou & Williams, 2016; Torres et al., 2020) and record breaking BB events in the SH (Hirsch & Koren, 2021) comes an increase in BrC emissions. These aerosol emissions have the potential to be deposited on snow and ice and contribute to global SDE and cryosphere decline. Absorption from BrC may have a larger impact on surface forcing than previously thought, with contributions comparable to BC. Low confidence in BrC forcing hinges on a dearth of model simulations that simulate BrC in the atmosphere and deposited on snow. Additional modeling studies that include a variation in BrC absorption properties on snow in addition to complex aerosol-snow feedbacks are necessary to better understand the role of BrC in the climate and cryosphere.

Acknowledgments, Samples, and Data

This work was supported in part by: the “Enabling Aerosol-cloud

interactions at GLobal convection-permitting scalES (EAGLES)” project (74358)

funded by the DOE Office of Science, Office of Biological and Environmental

Research, Earth System Model Development (ESMD) program, the U.S. Department of Energy (DOE), Office of Science, Office of Workforce Development for Teachers and Scientists, Office of Science Graduate Student Research (SCGSR) program, and the DOE as the

NSF, DOE, and USDA Joint Earth System Modeling (EaSM) Program. M. Wu is supported by the US Department of Energy (DOE), Office of Biological and Environmental Research, Earth and Environmental System Modeling program as part of the Energy Exascale Earth System Model (E3SM) project. The Pacific Northwest National Laboratory (PNNL) is operated for DOE by the Battelle Memorial Institute under contract DE-AC05-76RLO1830. All of the model source code and input data is archived on the GLADE file system, managed by the Computational and Information Systems Lab (CISL) of NCAR, and is available upon request from H. Wang (hailong.wang@pnnl.gov) and X. Liu (xiaohong.liu@tamu.edu). Plotting scripts for the figures in this document can be found on the Figshare website (https://figshare.com/s/c63f2a449907a906f455). The authors would like to acknowledge Sarah Doherty and Paolo Tuccella for sharing data used in the model validation. The authors would also like to acknowledge the use of computational resources (doi:10.5065/D6RX99HX) at the NCAR-Wyoming Supercomputing Center provided by the National Science Foundation and the State of Wyoming, and supported by NCAR's Computational and Information Systems Laboratory. We claim no potential conflicts of interest against any organization.

References

Abatzoglou, J. T., & Williams, A. P. (2016). Impact of anthropogenic climate change on wildfire across western US forests. *Proceedings of the National Academy of Sciences*, *113*(42), 11770–11775. https://doi.org/10.1073/pnas.1607171113Adler, G., Wagner, N. L., Lamb, K. D., Manfred, K. M., Schwarz, J. P., Franchin, A., et al. (2019). Evidence in biomass burning smoke for a light-absorbing aerosol with properties intermediate between brown and black carbon. *Aerosol Science and Technology*, *53*(9), 976–989. https://doi.org/10.1080/02786826.2019.1617832Albani, S., Mahowald, N. M., Perry, A. T., Scanza, R. A., Zender, C. S., Heavens, N. G., et al. (2014). Improved dust representation in the Community Atmosphere Model. *Journal of Advances in Modeling Earth Systems*, *6*(3), 541–570. https://doi.org/10.1002/2013MS000279Beres, N. D., Sengupta, D., Samburova, V., Khlystov, A. Y., & Moosmüller, H. (2020). Deposition of brown carbon onto snow: changes in snow optical and radiative properties. *Atmospheric Chemistry and Physics*, *20*(10), 6095–6114. https://doi.org/10.5194/acp-20-6095-2020Bond, T. C., Doherty, S. J., Fahey, D. W., Forster, P. M., Berntsen, T., DeAngelo, B. J., et al. (2013). Bounding the role of black carbon in the climate system: A scientific assessment. *Journal of Geophysical Research: Atmospheres*, *118*(11), 5380–5552. https://doi.org/10.1002/jgrd.50171Brown, H., Liu, X., Feng, Y., Jiang, Y., Wu, M., Lu, Z., et al. (2018). Radiative effect and climate impacts of brown carbon with the Community Atmosphere Model (CAM5). *Atmospheric Chemistry and Physics*, *18*(24), 17745–17768. https://doi.org/10.5194/acp-18-17745-2018Brown, H., Liu, X., Pokhrel, R., Murphy, S., Lu, Z., Saleh, R., et al. (2021). Biomass burning aerosols in most climate models are too absorbing. *Nature Communications*, *12*(1), 277. https://doi.org/10.1038/s41467-020-20482-9Boucher, O. *et al.* Clouds and

Aerosols. In: *Climate Change 2013: The Physical Science Basis. Contribution of Working Group I to the Fifth Assessment Report of the Intergovernmental Panel on Climate Change* [Stocker, T.F., D. Qin, G.-K. Plattner, M. Tignor, S.K. Allen, J. Boschung, A. Nauels, Y. Xia, V. Bex and P.M. Midgley (eds.)]. Cambridge University Press, Cambridge, United Kingdom and New York, NY, USA (2013).Clarke, A. D., & Noone, K. J. (1985). Soot in the Arctic snowpack: a cause for perturbations in radiative transfer. *Atmospheric Environment*, *19*, 2045–2053. https://doi.org/10.1016/0004-6981(85)90113-1Dang, C., Brandt, R. E., & Warren, S. G. (2015). Parameterizations for narrowband and broadband albedo of pure snow and snow containing mineral dust and black carbon. *Journal of Geophysical Research: Atmospheres*, *120*(11), 5446–5468. https://doi.org/10.1002/2014JD022646Doherty, S. J., Warren, S. G., Grenfell, T. C., Clarke, A. D., & Brandt, R. E. (2010). Light-absorbing impurities in Arctic snow. *Atmos. Chem. Phys.*, *10*(23), 11647–11680. https://doi.org/10.5194/acp-10-11647-2010Doherty, S. J., Dang, C., Hegg, D. A., Zhang, R., & Warren, S. G. (2014). Black carbon and other light-absorbing particles in snow of central North America: Black carbon in North American snow. *Journal of Geophysical Research: Atmospheres*, *119*(22), 12,807-12,831. https://doi.org/10.1002/2014JD022350Feng, L., Smith, S. J., Braun, C., Crippa, M., Gidden, M. J., Hoesly, R., et al. (2020). The generation of gridded emissions data for CMIP6. *Geoscientific Model Development*, *13*(2), 461–482. https://doi.org/10.5194/gmd-13-461-2020Flanner, M. G., Zender, C. S., Randerson, J. T., & Rasch, P. J. (2007). Present-day climate forcing and response from black carbon in snow. *Journal of Geophysical Research*, *112*(D11). https://doi.org/10.1029/2006JD008003Flanner, M. G., Zender, C. S., Hess, P. G., Mahowald, N. M., Painter, T. H., Ramanathan, V., & Rasch, P. J. (2009). Springtime warming and reduced snow cover from carbonaceous particles. *Atmospheric Chemistry and Physics*, *9*(7), 2481–2497. https://doi.org/10.5194/acp-9-2481-2009Flanner, M. G., Liu, X., Zhou, C., Penner, J. E., & Jiao, C. (2012). Enhanced solar energy absorption by internally-mixed black carbon in snow grains. *Atmospheric Chemistry and Physics*, *12*(10), 4699–4721. https://doi.org/10.5194/acp-12-4699-2012Forrister, H., Liu, J., Scheuer, E., Dibb, J., Ziemba, L., Thornhill, K. L., et al. (2015). Evolution of brown carbon in wildfire plumes. *Geophysical Research Letters*, *42*(11), 4623–4630. https://doi.org/10.1002/2015GL063897Gautam, R., Hsu, N. C., Lau, W. K.-M., & Yasunari, T. J. (2013). Satellite observations of desert dust-induced Himalayan snow darkening. *Geophysical Research Letters*, *40*(5), 988–993. https://doi.org/10.1002/grl.50226Gelaro, R., McCarty, W., Suárez, M. J., Todling, R., Molod, A., Takacs, L., et al. (2017). The Modern-Era Retrospective Analysis for Research and Applications, Version 2 (MERRA-2). *Journal of Climate*, *30*(14), 5419–5454. https://doi.org/10.1175/JCLI-D-16-0758.1Gettelman, A., Morrison, H., Santos, S., Bogenschutz, P., & Caldwell, P. M. (2015). Advanced Two-Moment Bulk Microphysics for Global Models. Part II: Global Model Solutions and Aerosol–Cloud Interactions*. *Journal of Climate*, *28*(3), 1288–1307. https://doi.org/10.1175/JCLI-D-14-00103.1Ghan, S. J., & Zaveri, R. A. (2007). Parameterization of optical properties for

hydrated internally mixed aerosol. *Journal of Geophysical Research*, *112*(D10). https://doi.org/10.1029/2006JD007927Hagler, G. S. W., Bergin, M. H., Smith, E. A., Dibb, J. E., Anderson, C., & Steig, E. J. (2007). Particulate and water-soluble carbon measured in recent snow at Summit, Greenland. *Geophysical Research Letters*, *34*(16). https://doi.org/10.1029/2007GL030110Hannay, C., & Neale, R. (2015). CAM5.4 simulations: The good, the bad and the ugly [presentation]. In *20th Annual CESM Workshop*. University Corporation For Atmospheric Research (UCAR):National Center for Atmospheric Research (NCAR):NCAR Earth System Laboratory (NESL):Climate and Global Dynamics Division (CGD): Breckenridge, CO, US.Hansen, J., Sato, M., Ruedy, R., Nazarenko, L., Lacis, A., Schmidt, G. A., et al. (2005). Efficacy of climate forcings. *Journal of Geophysical Research*, *110*(D18), D18104. https://doi.org/10.1029/2005JD005776Hansen, J., Sato, M., Ruedy, R., Kharecha, P., Lacis, A., Miller, R., et al. (2007). Climate simulations for 1880–2003 with GISS modelE. *Climate Dynamics*, *29*(7–8), 661–696. https://doi.org/10.1007/s00382-007-0255-8Hansen, James, & Nazarenko, L. (2004). Soot climate forcing via snow and ice albedos. *Proceedings of the National Academy of Sciences of the United States of America*, *101*(2), 423–428. https://doi.org/10.1073/pnas.2237157100He, C., Liou, K.-N., Takano, Y., Zhang, R., Levy Zamora, M., Yang, P., et al. (2015). Variation of the radiative properties during black carbon aging: theoretical and experimental intercomparison. *Atmospheric Chemistry and Physics*, *15*(20), 11967–11980. https://doi.org/10.5194/acp-15-11967-2015He, C., Liou, K., Takano, Y., Yang, P., Qi, L., & Chen, F. (2018a). Impact of Grain Shape and Multiple Black Carbon Internal Mixing on Snow Albedo: Parameterization and Radiative Effect Analysis. *Journal of Geophysical Research: Atmospheres*, *123*(2), 1253–1268. https://doi.org/10.1002/2017JD027752He, C., Flanner, M. G., Chen, F., Barlage, M., Liou, K.-N., Kang, S., et al. (2018b). Black carbon-induced snow albedo reduction over the Tibetan Plateau: uncertainties from snow grain shape and aerosol–snow mixing state based on an updated SNICAR model. *Atmospheric Chemistry and Physics*, *18*(15), 11507–11527. https://doi.org/10.5194/acp-18-11507-2018Hegg, D. A., Warren, S. G., Grenfell, T. C., Sarah J Doherty, & Clarke, A. D. (2010). Sources of light-absorbing aerosol in arctic snow and their seasonal variation. *Atmospheric Chemistry and Physics*, *10*(22), 10923–10938. https://doi.org/10.5194/acp-10-10923-2010Hess, M., Koepke, P., & Schult, I. (1998). Optical Properties of Aerosols and Clouds: The Software Package OPAC. *Bulletin of the American Meteorological Society*, *79*(5), 831–844. https://doi.org/10.1175/1520-0477(1998)079<0831:OPOAAC>2.0.CO;2Hirsch, E., & Koren, I. (2021). Record-breaking aerosol levels explained by smoke injection into the stratosphere. *Science*, *371*(6535), 1269–1274. https://doi.org/10.1126/science.abe1415Hock, R., G. Rasul, C. Adler, B. Cáceres, S. Gruber, Y. Hirabayashi, M. Jackson, A. Kääb, S. Kang, S. Kutuzov, Al. Milner, U. Molau, S. Morin, B. Orlove, and H. Steltzer, 2019: High Mountain Areas. In: *IPCC Special Report on the Ocean and Cryosphere in a Changing Climate* [H.-O. Pörtner, D.C. Roberts, V. Masson-Delmotte,

P. Zhai, M. Tignor, E. Poloczanska, K. Mintenbeck, A. Alegría, M. Nicolai, A. Okem, J. Petzold, B. Rama, N.M. Weyer (eds.)]. In press.Hoesly, R. M., Smith, S. J., Feng, L., Klimont, Z., Janssens-Maenhout, G., Pitkanen, T., et al. (2018). Historical (1750–2014) anthropogenic emissions of reactive gases and aerosols from the Community Emissions Data System (CEDS). *Geoscientific Model Development*, *11*(1), 369–408. https://doi.org/10.5194/gmd-11-369-2018Hugonnet, R., McNabb, R., Berthier, E., Menounos, B., Nuth, C., Girod, L., et al. (2021). Accelerated global glacier mass loss in the early twenty-first century. *Nature*, *592*(7856), 726–731. https://doi.org/10.1038/s41586-021-03436-zHurrell, J. W., Hack, J. J., Shea, D., Caron, J. M., & Rosinski, J. (2008). A New Sea Surface Temperature and Sea Ice Boundary Dataset for the Community Atmosphere Model. *Journal of Climate*, *21*(19), 5145–5153. https://doi.org/10.1175/2008JCLI2292.1Jacobson, M. Z. (2012). Investigating cloud absorption effects: Global absorption properties of black carbon, tar balls, and soil dust in clouds and aerosols. *Journal of Geophysical Research: Atmospheres*, *117*(D6), n/a-n/a. https://doi.org/10.1029/2011JD017218Jiao, C., Flanner, M. G., Balkanski, Y., Bauer, S. E., Bellouin, N., Berntsen, T. K., et al. (2014). An AeroCom assessment of black carbon in Arctic snow and sea ice. *Atmospheric Chemistry and Physics*, *14*(5), 2399–2417. https://doi.org/10.5194/acp-14-2399-2014Koch, D., Menon, S., Del Genio, A., Ruedy, R., Alienov, I., & Schmidt, G. A. (2009). Distinguishing Aerosol Impacts on Climate over the Past Century. *Journal of Climate*, *22*(10), 2659–2677. https://doi.org/10.1175/2008JCLI2573.1Krishnan, R., Sabin, T. P., Vellore, R., Mujumdar, M., Sanjay, J., Goswami, B. N., et al. (2016). Deciphering the desiccation trend of the South Asian monsoon hydroclimate in a warming world. *Climate Dynamics*, *47*(3–4), 1007–1027. https://doi.org/10.1007/s00382-015-2886-5Laskin, A., Laskin, J., & Nizkorodov, S. A. (2015). Chemistry of Atmospheric Brown Carbon. *Chemical Reviews*, *115*(10), 4335–4382. https://doi.org/10.1021/cr5006167Lawrence, D. M., Oleson, K. W., Flanner, M. G., Fletcher, C. G., Lawrence, P. J., Levis, S., et al. (2012). The CCSM4 Land Simulation, 1850–2005: Assessment of Surface Climate and New Capabilities. *Journal of Climate*, *25*(7), 2240–2260. https://doi.org/10.1175/JCLI-D-11-00103.1Li, C., He, Q., Hettiyadura, A. P. S., Käfer, U., Shmul, G., Meidan, D., et al. (2020). Formation of Secondary Brown Carbon in Biomass Burning Aerosol Proxies through NO3 Radical Reactions. *Environmental Science & Technology*, *54*(3), 1395–1405. https://doi.org/10.1021/acs.est.9b05641Lin, G., Penner, J. E., Flanner, M. G., Sillman, S., Xu, L., & Zhou, C. (2014). Radiative forcing of organic aerosol in the atmosphere and on snow: Effects of SOA and brown carbon. *Journal of Geophysical Research: Atmospheres*, *119*(12), 7453–7476. https://doi.org/10.1002/2013JD021186Lin, P., Bluvshtein, N., Rudich, Y., Nizkorodov, S. A., Laskin, J., & Laskin, A. (2017). Molecular Chemistry of Atmospheric Brown Carbon Inferred from a Nationwide Biomass Burning Event. *Environmental Science & Technology*, *51*(20), 11561–11570. https://doi.org/10.1021/acs.est.7b02276Liu, D., He, C., Schwarz, J. P., & Wang, X. (2020). Lifecycle of light-absorbing carbonaceous aerosols in the atmosphere. *Npj Climate and Atmospheric Science*, *3*(1), 40.

https://doi.org/10.1038/s41612-020-00145-8Liu, X., Easter, R. C., Ghan, S. J., Zaveri, R., Rasch, P., Shi, X., et al. (2012). Toward a minimal representation of aerosols in climate models: description and evaluation in the Community Atmosphere Model CAM5. *Geoscientific Model Development*, *5*(3), 709–739. https://doi.org/10.5194/gmd-5-709-2012Liu, X., Ma, P.-L., Wang, H., Tilmes, S., Singh, B., Easter, R. C., et al. (2016). Description and evaluation of a new four-mode version of the Modal Aerosol Module (MAM4) within version 5.3 of the Community Atmosphere Model. *Geoscientific Model Development*, *9*(2), 505–522. https://doi.org/10.5194/gmd-9-505-2016Meredith, M., Sommerkorn, M., Cassotta, S., Derksen, C., Ekaykin, A., Hollowed, A., Kofinas, G., Mackintosh, A., Melbourne- Thomas, J., Muelbert, M. M. C., Ottersen, G., Pritchard, H., and Schuur, E. A. G.: Polar Regions, in: IPCC Special Report on the Ocean and Cryosphere in a Changing Climate, edited by: Pörtner, H.-O., Roberts, D. C., Masson-Delmotte, V., Zhai, P., Tignor, M., Poloczanska, E., Mintenbeck, K., Alegría, A., Nicolai, M., Okem, A., Petzold, J., Rama, B., and Weyer, N. M., in press, 2019.Ming, J., Wang, P., Zhao, S., & Chen, P. (2013). Disturbance of light-absorbing aerosols on the albedo in a winter snowpack of Central Tibet. *Journal of Environmental Sciences*, *25*(8), 7.Morrison, H., & Gettelman, A. (2008). A New Two-Moment Bulk Stratiform Cloud Microphysics Scheme in the Community Atmosphere Model, Version 3 (CAM3). Part I: Description and Numerical Tests. *Journal of Climate*, *21*(15), 3642–3659. https://doi.org/10.1175/2008JCLI2105.1Neale, R. B., *et al.* Description of the NCAR Community Atmosphere Model (CAM 5.0), NCAR Tech. Note NCAR/TN-486+STR, 289 pp., Natl. Cent. for Atmos. Res, Boulder, CO, USA (2012).Nerem, R. S., Beckley, B. D., Fasullo, J. T., Hamlington, B. D., Masters, D., & Mitchum, G. T. (2018). Climate-change–driven accelerated sea-level rise detected in the altimeter era. *Proceedings of the National Academy of Sciences*, *115*(9), 2022–2025. https://doi.org/10.1073/pnas.1717312115Oleson, K. W. *et al.* Technical description of version 4.0 of the Community Land Model, NCAR Tech. Note NCAR/TN-478+STR (2010). Painter, T. H., Barrett, A. P., Landry, C. C., Neff, J. C., Cassidy, M. P., Lawrence, C. R., et al. (2007). Impact of disturbed desert soils on duration of mountain snow cover. *Geophysical Research Letters*, *34*(12), L12502. https://doi.org/10.1029/2007GL030284Painter, T. H., Bryant, A. C., & Skiles, S. M. (2012). Radiative forcing by light absorbing impurities in snow from MODIS surface reflectance data. *Geophysical Research Letters*, *39*(17), n/a-n/a. https://doi.org/10.1029/2012GL052457Potenza, M. A. C., Albani, S., Delmonte, B., Villa, S., Sanvito, T., Paroli, B., et al. (2016). Shape and size constraints on dust optical properties from the Dome C ice core, Antarctica. *Scientific Reports*, *6*(1), 28162. https://doi.org/10.1038/srep28162Qian, Y., Wang, H., Zhang, R., Flanner, M. G., & Rasch, P. J. (2014). A sensitivity study on modeling black carbon in snow and its radiative forcing over the Arctic and Northern China. *Environmental Research Letters*, *9*(6), 064001. https://doi.org/10.1088/1748-9326/9/6/064001Rahimi, S., Liu, X., Wu, C., Lau, W. K., Brown, H., Wu, M., & Qian, Y. (2019). Quantifying snow darkening and atmospheric radiative effects of black carbon and dust on the

South Asian monsoon and hydrological cycle: experiments using variable-resolution CESM. *Atmospheric Chemistry and Physics*, *19*(18), 12025–12049. https://doi.org/10.5194/acp-19-12025-2019Rahimi, S., Liu, X., Zhao, C., Lu, Z., & Lebo, Z. J. (2020). Examining the atmospheric radiative and snow-darkening effects of black carbon and dust across the Rocky Mountains of the United States using WRF-Chem. *Atmospheric Chemistry and Physics*, *20*(18), 10911–10935. https://doi.org/10.5194/acp-20-10911-2020Ren, L., Yang, Y., Wang, H., Zhang, R., Wang, P., & Liao, H. (2020). Source attribution of Arctic black carbon and sulfate aerosols and associated Arctic surface warming during 1980–2018. *Atmospheric Chemistry and Physics*, *20*(14), 9067–9085. https://doi.org/10.5194/acp-20-9067-2020de Sá, S. S., Rizzo, L. V., Palm, B. B., Campuzano-Jost, P., Day, D. A., Yee, L. D., et al. (2019). Contributions of biomass-burning, urban, and biogenic emissions tothe concentrations and light-absorbing properties of particulatematter in central Amazonia during the dry season. *Atmospheric Chemistry and Physics Discussions*, 1–77. https://doi.org/10.5194/acp-2018-1309Saleh, R. (2020). From Measurements to Models: Toward Accurate Representation of Brown Carbon in Climate Calculations. *Current Pollution Reports*. https://doi.org/10.1007/s40726-020-00139-3Saleh, R., Robinson, E. S., Tkacik, D. S., Ahern, A. T., Liu, S., Aiken, A. C., et al. (2014). Brownness of organics in aerosols from biomass burning linked to their black carbon content. *Nature Geoscience*, *7*(9), 647–650. https://doi.org/10.1038/ngeo2220Saleh, R., Cheng, Z., & Atwi, K. (2018). The Brown–Black Continuum of Light-Absorbing Combustion Aerosols. *Environmental Science & Technology Letters*, *5*(8), 508–513. https://doi.org/10.1021/acs.estlett.8b00305Schwarz, J. P., Gao, R. S., Perring, A. E., Spackman, J. R., & Fahey, D. W. (2013). Black carbon aerosol size in snow. *Scientific Reports*, *3*(1), 1356. https://doi.org/10.1038/srep01356Skeie, R. B., Berntsen, T. K., Myhre, G., Tanaka, K., Kvalevåg, M. M., & Hoyle, C. R. (2011). Anthropogenic radiative forcing time series from pre-industrial times until 2010. *Atmospheric Chemistry and Physics*, *11*(22), 11827–11857. https://doi.org/10.5194/acp-11-11827-2011Skiles, S. M., Painter, T. H., Deems, J. S., Bryant, A. C., & Landry, C. C. (2012). Dust radiative forcing in snow of the Upper Colorado River Basin: 2. Interannual variability in radiative forcing and snowmelt rates: DUST RADIATIVE FORCING SNOWMELT RESPONSE. *Water Resources Research*, *48*(7). https://doi.org/10.1029/2012WR011986Tedesco, M., Fettweis, X., van den Broeke, M. R., van de Wal, R. S. W., Smeets, C. J. P. P., van de Berg, W. J., et al. (2011). The role of albedo and accumulation in the 2010 melting record in Greenland. *Environmental Research Letters*, *6*(1), 014005. https://doi.org/10.1088/1748-9326/6/1/014005Torres, O., Bhartia, P. K., Taha, G., Jethva, H., Das, S., Colarco, P., et al. (2020). Stratospheric Injection of Massive Smoke Plume From Canadian Boreal Fires in 2017 as Seen by DSCOVR-EPIC, CALIOP, and OMPS-LP Observations. *Journal of Geophysical Research: Atmospheres*, *125*(10). https://doi.org/10.1029/2020JD032579Tuccella, P., Pitari, G., Colaiuda, V., Raparelli, E., & Curci, G. (2021). Present-day radiative effect from radiation-

absorbing aerosols in snow. *Atmospheric Chemistry and Physics*, *21*(9), 6875–6893. https://doi.org/10.5194/acp-21-6875-2021Wang, H., Rasch, P. J., Easter, R. C., Singh, B., Zhang, R., Ma, P.-L., et al. (2014). Using an explicit emission tagging method in global modeling of source-receptor relationships for black carbon in the Arctic: Variations, sources, and transport pathways: Source attribution of BC in the Arctic. *Journal of Geophysical Research: Atmospheres*, *119*(22), 12,888-12,909. https://doi.org/10.1002/2014JD022297Wang, H., Easter, R. C., Zhang, R., Ma, P., Singh, B., Zhang, K., et al. (2020). Aerosols in the E3SM Version 1: New Developments and Their Impacts on Radiative Forcing. *Journal of Advances in Modeling Earth Systems*, *12*(1). https://doi.org/10.1029/2019MS001851Wang, M., Xu, B., Cao, J., Tie, X., Wang, H., Zhang, R., et al. (2015). Carbonaceous aerosols recorded in a southeastern Tibetan glacier: analysis of temporal variations and model estimates of sources and radiative forcing. *Atmospheric Chemistry and Physics*, *15*(3), 1191–1204. https://doi.org/10.5194/acp-15-1191-2015Wang, X., Heald, C. L., Sedlacek, A. J., de Sá, S. S., Martin, S. T., Alexander, M. L., et al. (2016). Deriving brown carbon from multiwavelength absorption measurements: method and application to AERONET and Aethalometer observations. *Atmos. Chem. Phys.*, *16*(19), 12733–12752. https://doi.org/10.5194/acp-16-12733-2016Wang, X., Heald, C. L., Liu, J., Weber, R. J., Campuzano-Jost, P., Jimenez, J. L., et al. (2018). Exploring the observational constraints on the simulation of brown carbon. *Atmos. Chem. Phys.*, *18*(2), 635–653. https://doi.org/10.5194/acp-18-635-2018Wang, Xin, Doherty, S. J., & Huang, J. (2013). Black carbon and other light-absorbing impurities in snow across Northern China. *Journal of Geophysical Research: Atmospheres*, *118*(3), 1471–1492. https://doi.org/10.1029/2012JD018291Ward, J. L., Flanner, M. G., Bergin, M., Dibb, J. E., Polashenski, C. M., Soja, A. J., & Thomas, J. L. (2018). Modeled Response of Greenland Snowmelt to the Presence of Biomass Burning-Based Absorbing Aerosols in the Atmosphere and Snow. *Journal of Geophysical Research: Atmospheres*, *123*(11), 6122–6141. https://doi.org/10.1029/2017JD027878Warren, S. G. (1984). Impurities in Snow: Effects on Albedo and Snowmelt (Review). *Annals of Glaciology*, *5*, 177–179. https://doi.org/10.3189/1984AoG5-1-177-179Warren, S. G. (2013). Can black carbon in snow be detected by remote sensing? *Journal of Geophysical Research: Atmospheres*, *118*(2), 779–786. https://doi.org/10.1029/2012JD018476Warren, S. G., & Wiscombe, W. J. (1980). A Model for the Spectral Albedo of Snow. II: Snow Containing Atmospheric Aerosols. *Journal of the Atmospheric Sciences*, *37*(12), 2734–2745. https://doi.org/10.1175/1520-0469(1980)037<2734:AMFTSA>2.0.CO;2van der Werf, G. R., Randerson, J. T., Giglio, L., Leeuwen, T. T. van, Chen, Y., Rogers, B. M., et al. (2017). Global fire emissions estimates during 1997–2016. *Earth System Science Data*, *9*(2), 697–720. https://doi.org/10.5194/essd-9-697-2017Wu, C., Liu, X., Lin, Z., Rahimi-Esfarjani, S. R., & Lu, Z. (2018). Impacts of absorbing aerosol deposition on snowpack and hydrologic cycle in the Rocky Mountain region based on variable-resolution CESM (VR-CESM) simulations. *Atmospheric Chemistry and Physics*, *18*(2), 511–533.

https://doi.org/10.5194/acp-18-511-2018Wu, M., Liu, X., Yang, K., Luo, T., Wang, Z., Wu, C., et al. (2019). Modeling Dust in East Asia by CESM and Sources of Biases. *Journal of Geophysical Research: Atmospheres*, *124*(14), 8043–8064. https://doi.org/10.1029/2019JD030799Xu, B., Cao, J., Hansen, J., Yao, T., Joswia, D. R., Wang, N., et al. (2009). Black soot and the survival of Tibetan glaciers. *Proceedings of the National Academy of Sciences*, *106*(52), 22114–22118.Yang, Y., Wang, H., Smith, S. J., Ma, P.-L., & Rasch, P. J. (2017). Source attribution of black carbon and its direct radiative forcing in China. *Atmospheric Chemistry and Physics*, *17*(6), 4319–4336. https://doi.org/10.5194/acp-17-4319-2017Yang, Y., Wang, H., Smith, S. J., Zhang, R., Lou, S., Qian, Y., et al. (2018a). Recent intensification of winter haze in China linked to foreign emissions and meteorology. *Scientific Reports*, *8*(1), 2107. https://doi.org/10.1038/s41598-018-20437-7Yang, Y., Wang, H., Smith, S. J., Zhang, R., Lou, S., Yu, H., et al. (2018b). Source Apportionments of Aerosols and Their Direct Radiative Forcing and Long-Term Trends Over Continental United States. *Earth's Future*, *6*(6), 793–808. https://doi.org/10.1029/2018EF000859Yang, Y., Lou, S., Wang, H., Wang, P., & Liao, H. (2020). Trends and source apportionment of aerosols in Europe during 1980–2018. *Atmospheric Chemistry and Physics*, *20*(4), 2579–2590. https://doi.org/10.5194/acp-20-2579-2020Yasunari, T. J., Aoki, T., Aoki, K., Murao, N., Yamagata, S., & Kodama, Y. (2014). The GOddard SnoW Impurity Module (GOSWIM) for the NASA GEOS-5 Earth System Model: Preliminary Comparisons with Observations in Sapporo, Japan. *SOLA*, *10*, 8.Zhang, R., Wang, H., Hegg, D. A., Qian, Y., Doherty, S. J., Dang, C., et al. (2015a). Quantifying sources of black carbon in Western North America using observationally based analysis and an emission tagging technique in the Community Atmosphere Model. *Atmospheric Chemistry and Physics Discussions*, *15*(9), 12957–13000. https://doi.org/10.5194/acpd-15-12957-2015Zhang, R., Wang, H., Qian, Y., Rasch, P. J., Easter, R. C., Ma, P.-L., et al. (2015b). Quantifying sources, transport, deposition, and radiative forcing of black carbon over the Himalayas and Tibetan Plateau. *Atmospheric Chemistry and Physics*, *15*(11), 6205–6223. https://doi.org/10.5194/acp-15-6205-2015Zhong, M., & Jang, M. (2014). Dynamic light absorption of biomass-burning organic carbon photochemically aged under natural sunlight. *Atmos. Chem. Phys.*, *14*(3), 1517–1525. https://doi.org/10.5194/acp-14-1517-2014

Journal of Advances in Modeling Earth Systems (JAMES)

Supporting Information for

Brown Carbon Fuel and Emission Source Attributions to Global Snow Darkening Effect

Hunter Brown[1,2], Hailong Wang[3], Mark Flanner[4], Xiaohong Liu[2], Balwinder Singh[3], Rudong Zhang[3], Yang Yang[5], Mingxuan Wu[3]

[1]Department of Atmospheric Science, University of Wyoming, Laramie, WY, USA.

[2]Department of Atmospheric Sciences, Texas A&M University, College Station, TX, USA.

[3]Atmospheric Sciences and Global Change Division, Pacific Northwest National Laboratory, Richland, WA, USA.

[4]Department of Atmospheric, Oceanic and Space Sciences, University of Michigan, Ann Arbor MI, USA

[5]Jiangsu Key Laboratory of Atmospheric Environment Monitoring and Pollution Control, Jiangsu Collaborative Innovation Center of Atmospheric Environment and Equipment Technology, School of Environmental Science and Engineering, Nanjing University of Information Science and Technology, Nanjing, Jiangsu, China

Contents of this file

Introduction

The goal of this supplementary is to add additional information regarding the analyses presented in the main text. This includes the tabulated data and methods used when comparing model data to collected snow samples (in Fig. 2 in main text), the equation used for temporal cross correlation (in Fig. 10 in main text), a flow chart describing the incorporation of brown carbon (BrC) in SNICAR (in section 2.2.3 in main text), and additional plots that support the conclusions in the main text.

Observational data is collected from Doherty et al. (2010), Wang et al. (2013), and Doherty et al. (2014). All model comparisons are generated using the same CESM tagging implementation and brown carbon parameterization described in the main text. The GEOS-Chem model mass absorption cross section (MAC) is from Tuccella et al. (2021), while the brown carbon MAC are derived from a 1-year simulation for the year 2005. Other model analyses are based on the same three simulations described in the main text (i.e., BRC, BRC_PB, and NOBRC). These additional analysis include: the difference and ratio between BrC snow darkening effect (SDE) with different model treatments; source contributions to BrC SDE with photochemical bleaching; comparison of regional SDE and deposition for different light absorbing species; seasonal variation SDE and variables affecting SDE calculation; and the modeled sea-ice surface area in the Arctic and Antarctic.

Model Validation S1.

Model data is selected from grid cells and monthly time stamps that correspond to the collection dates and latitude-longitude of the observations. Modeled BC snow surface concentration (ng g^{-1}) from the BRC simulation is used to compare to C_{BC} (Fig. 2a). Due to the similarities between filter absorption measurements and the impact of absorbing aerosol on snow albedo, the ratio of modeled dust and OC SDE to total aerosol SDE ($(SDE_{dust}+SDE_{OC})/(SDE_{aer})$) is used as a comparison to $f_{non\text{-}BC}$ (Fig. 2b). Samples were neglected in cases where there was no snow in the model corresponding to the sample dates in the observations (i.e., SDE = 0) and where underlying snow surfaces in the model were darkened to such a degree that $SDE_{dust}+SDE_{OC}$ or SDE_{aer} was negative (i.e., non-physical $f_{non\text{-}BC}$).

Cross-correlation Coefficient S2.

The following equation is used to calculate the Pearson sample linear cross-correlation coefficients at lag 0 (TCC) between BrC SDE (X) and the various mechanisms that impact calculation of BrC SDE (Y),

$$TCC = \frac{1}{N-1} \frac{\sum_{i=1}^{N}(X_i - \overline{X})(Y_i - \overline{Y})}{\sqrt{\frac{\sum_{i=1}^{N}(X_i - \overline{X})^2}{N-1}} \sqrt{\frac{\sum_{i=1}^{N}(Y_i - \overline{Y})^2}{N-1}}} = \frac{1}{N-1} \frac{\sum_{i=1}^{N}(X_i - \overline{X})(Y_i - \overline{Y})}{X_{std} Y_{std}} \quad \text{Eq. S1}$$

where N is months in the year, $\overline{X}$ is the annual mean BrC SDE, $\overline{Y}$ is the annual mean input to BrC SDE calculation, X_{std} is the standard deviation in monthly BrC SDE, and Y_{std} is the standard deviation in the monthly input to BrC SDE calculation.

References

Doherty, S. J., Warren, S. G., Grenfell, T. C., Clarke, A. D., & Brandt, R. E. (2010). Light-absorbing impurities in Arctic snow. *Atmos. Chem. Phys.*, *10*(23), 11647–11680. https://doi.org/10.5194/acp-10-11647-2010

Doherty, S. J., Dang, C., Hegg, D. A., Zhang, R., & Warren, S. G. (2014). Black carbon and other light-absorbing particles in snow of central North America: Black carbon in North American snow. *Journal of Geophysical Research: Atmospheres*, *119*(22), 12,807-12,831. https://doi.org/10.1002/2014JD022350

Wang, Xin, Doherty, S. J., & Huang, J. (2013). Black carbon and other light-absorbing impurities in snow across Northern China. *Journal of Geophysical Research: Atmospheres*, *118*(3), 1471–1492. https://doi.org/10.1029/2012JD018291

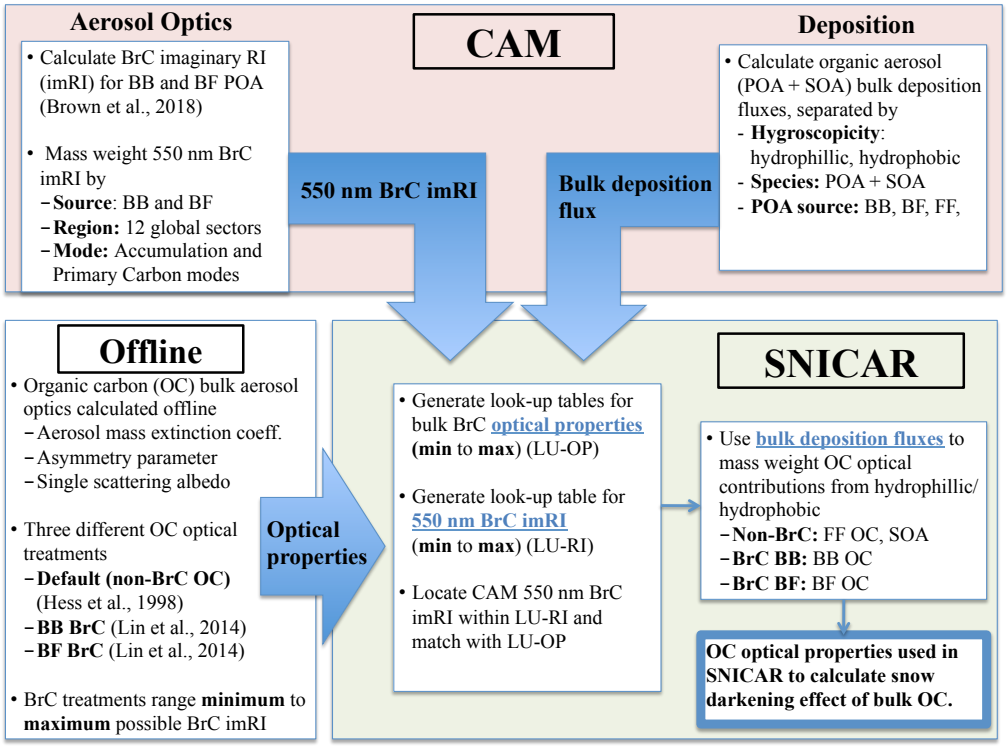

Figure S1. A visual depiction of the transfer of brown carbon (BrC) imaginary refractive index from the Community Atmosphere Model (CAM) to the Snow Ice and Aerosol Radiative (SNICAR) model within the Community Land Model (CLM).

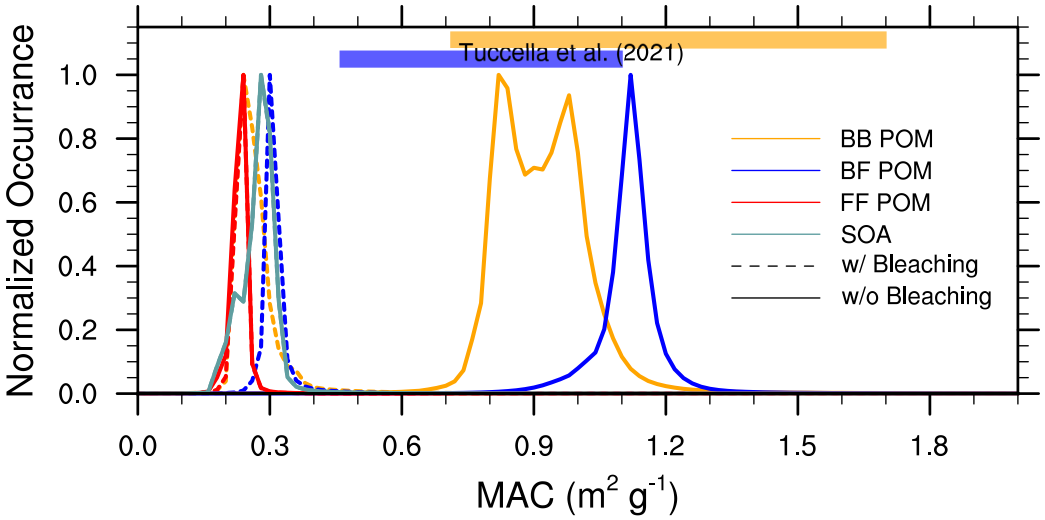

Figure S2. Mass absorption cross-section (MAC) of POM – both BrC and non-BrC – in CAM for the year 2005. The MAC are averaged over the visible spectrum (0.3-0.7 μm). Solid lines are from BRC simulations while dashed lines are from BRC_PB simulations. Prescribed BrC MAC from Tuccella et al. (2021),

from aged to fresh (left to right) are represented by solid bars at the top of the plot.

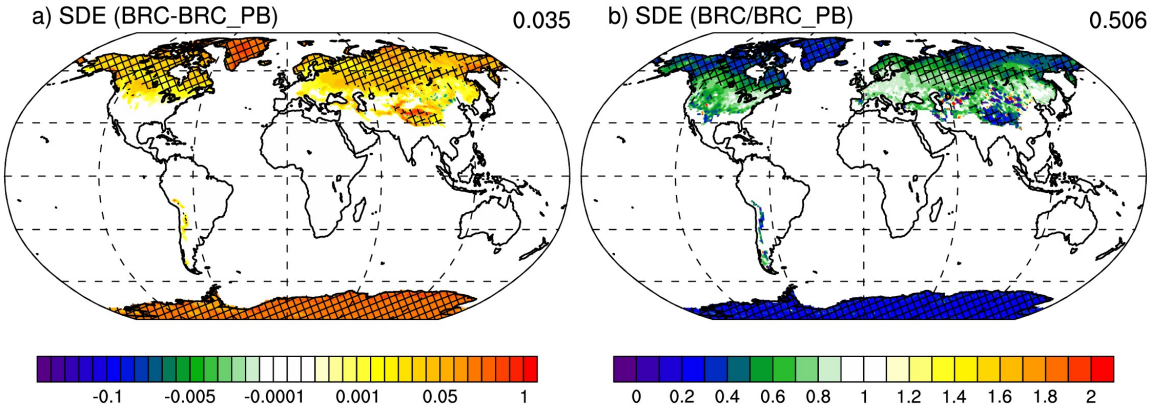

Figure S3. Global plot of the difference and ratio of BrC SDE. a) difference between BrC SDE from BRC and BRC_PB simulations (BRC-BRC_PB) and b) ratio of BrC SDE from BRC and BRC_PB simulations (BRC_PB/BRC). Hatching indicates grid cells where the change across the 10 simulation years is significant to the 0.1 level.

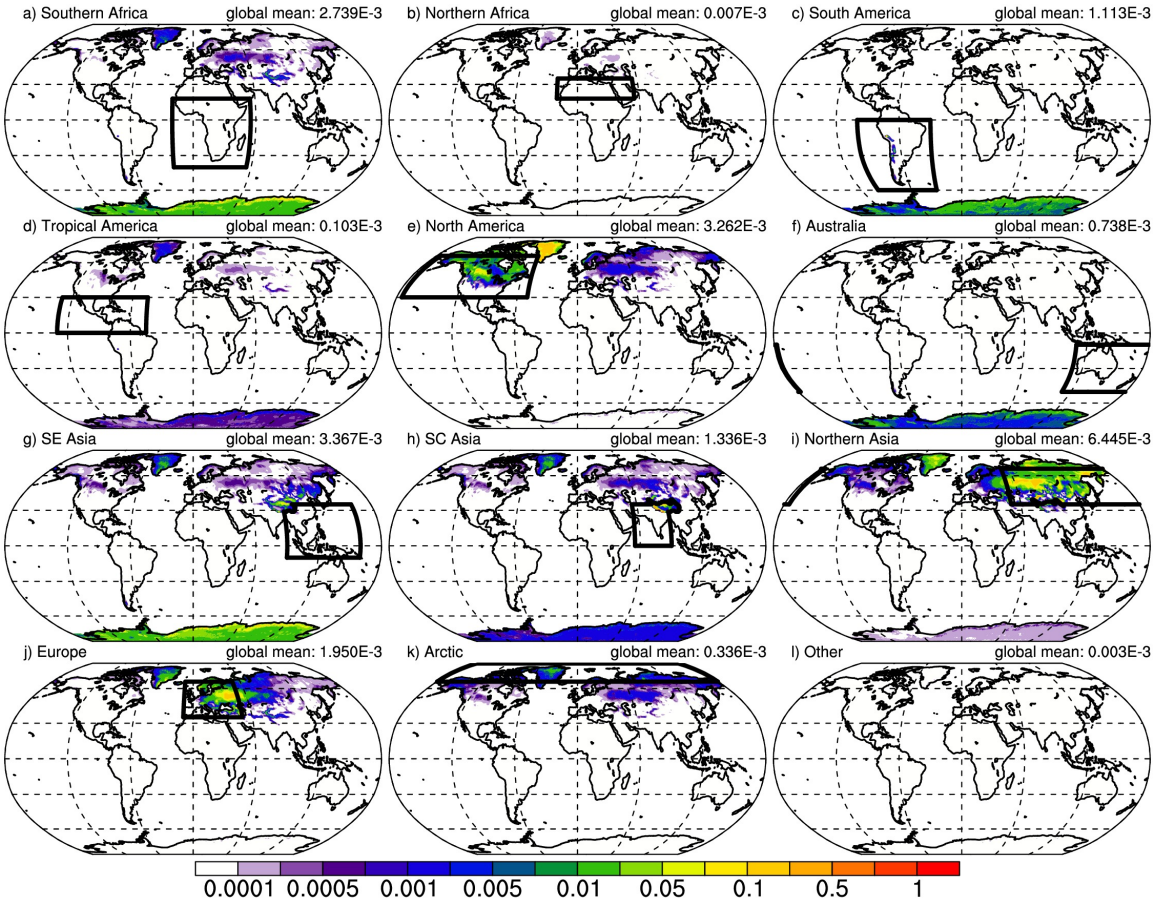

Figure S4. Regional contribution to the 10-year mean BrC snow darkening effect (SDE; W m^{-2}) from BB and BF sources. The SDE is from the BRC_PB simulation (bleaching BrC) so represents the lower bound for BrC contribution to SDE. Emission regions are marked in each panel with a solid black box and correspond to the regions in Fig. 1. The BrC SDE is averaged over all grid-cells, with and without snow cover.

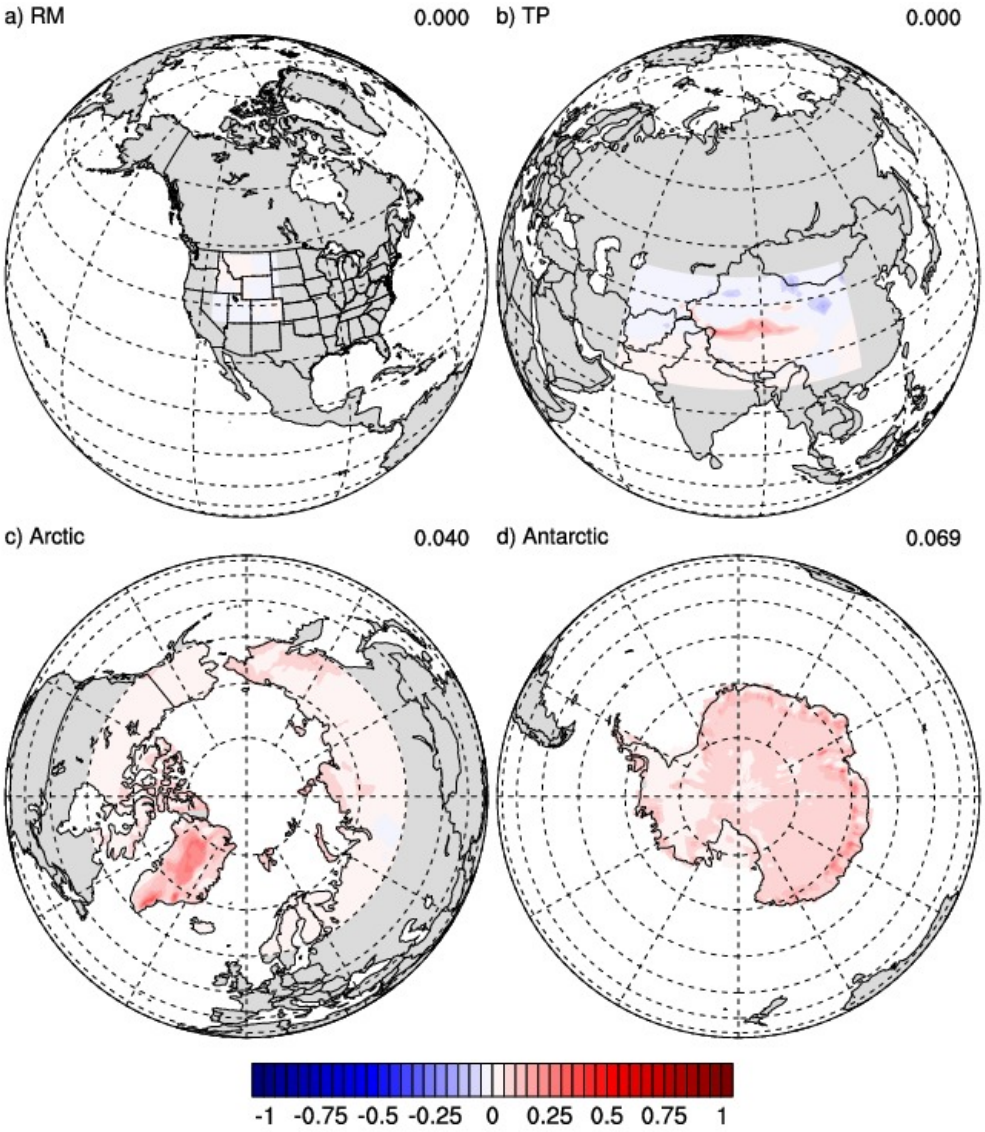

Figure S5. Same as Fig. 7 but showing SDE (W m^{-2}) from OC in the NOBRC simulation.

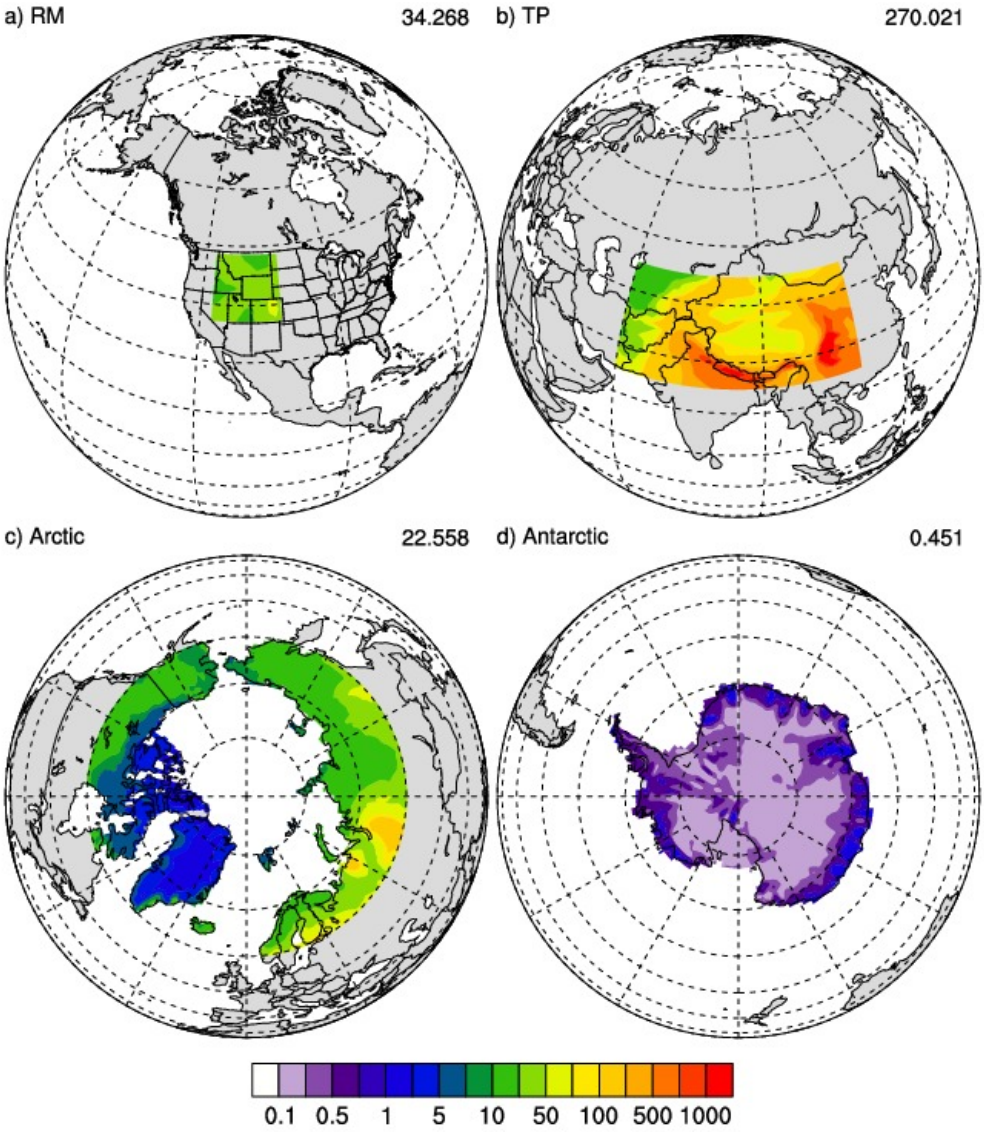

Figure S6. Same as Fig. S4 but showing BC deposition (ug m^{-2} day^{-1}).

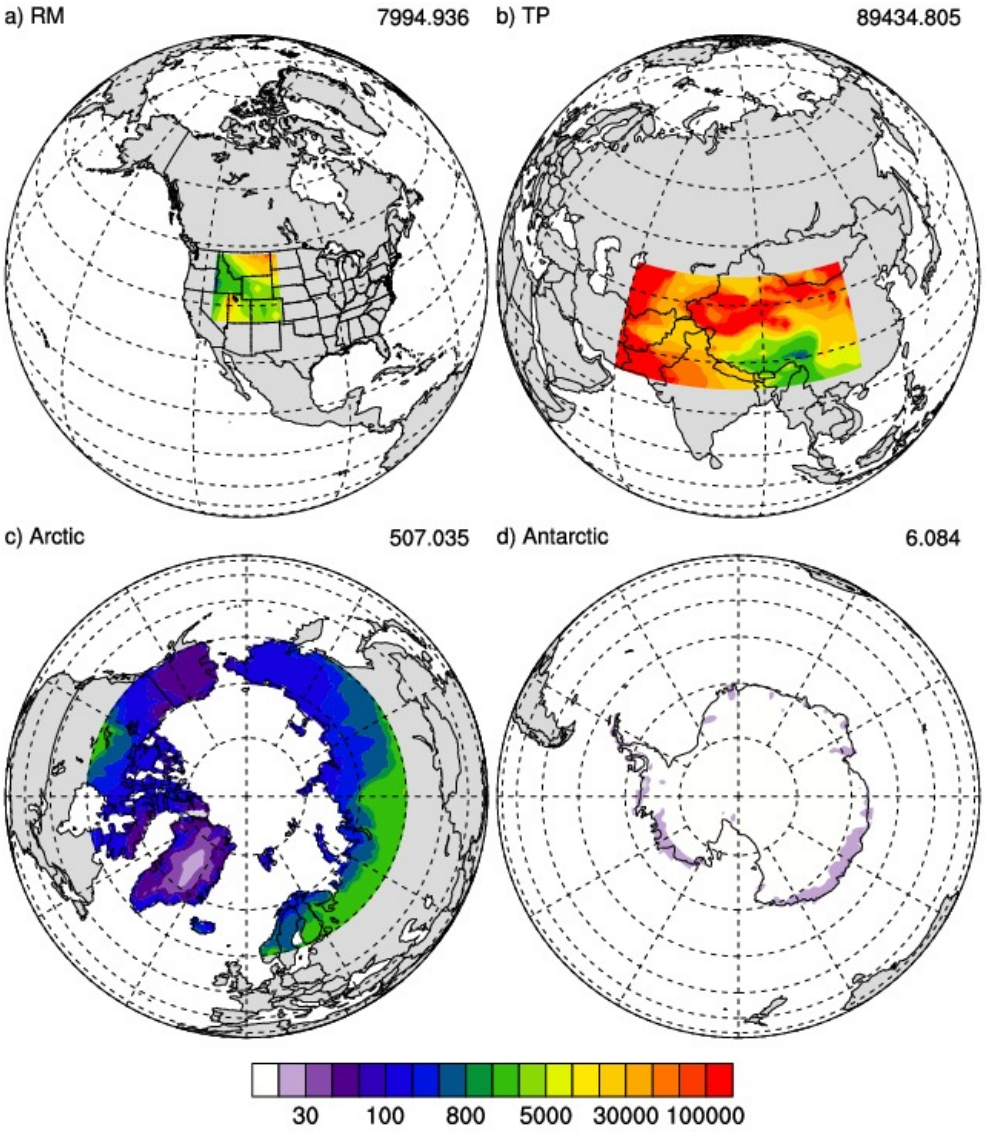

Figure S7. Same as Fig. S5 but showing dust deposition (ug m^{-2} day^{-1}). Note that the scale is increased 2 orders of magnitude from that of Fig. S5.

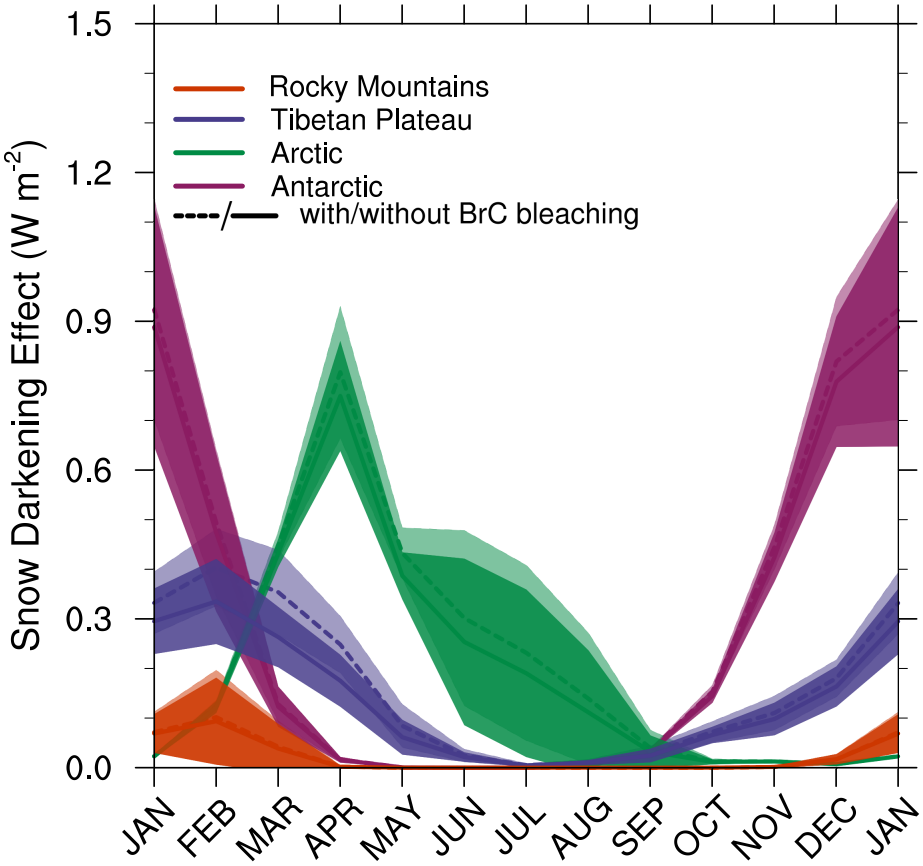

Figure S8. Monthly mean variation in 10-year mean BC + dust SDE (Wm^{-2}) from the four regions described in Fig. 8, ± one standard deviation. Colors represent the Rocky Mountains (orange), the Tibetan Plateau (purple), the Arctic (green), and the Antarctic (maroon). The BC+dust SDE is from the BRC and BRC_PB simulations and is averaged over all grid-cells, with and without snow cover.

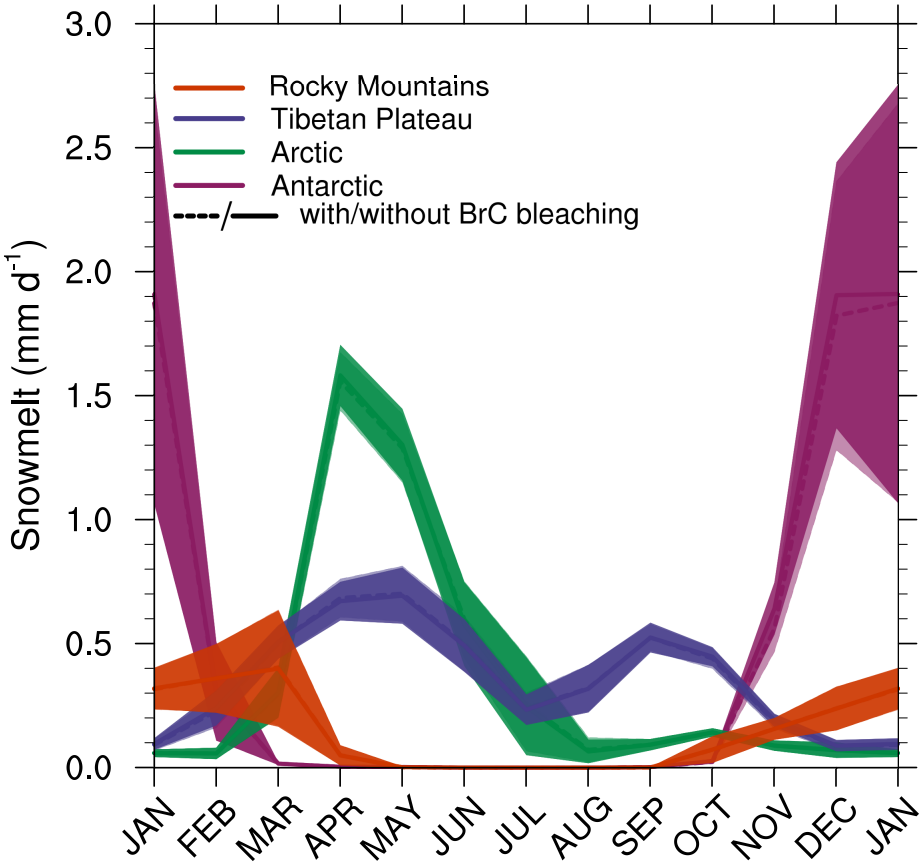

Figure S9. Monthly mean variation in 10-year mean snowmelt (mm d^{-1} from the four regions described in Fig. 8, ± one standard deviation. Colors represent the Rocky Mountains (orange), the Tibetan Plateau (purple), the Arctic (green), and the Antarctic (maroon). The snowmelt is from the BRC and BRC_PB simulations.

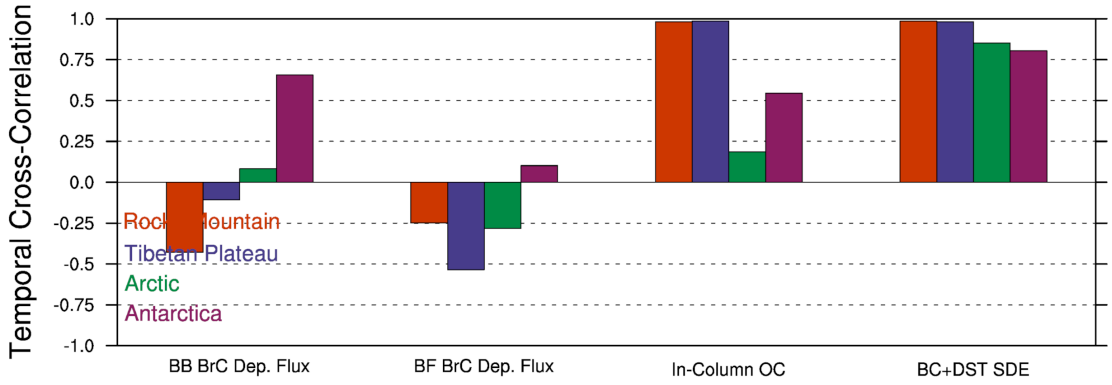

Figure S10. Temporal cross-correlation between monthly average BrC SDE and mechanisms that play into the calculation of SDE. These mechanisms are BB BrC deposition flux (kg m^{-2} s^{-1}), BF BrC deposition flux (kg m^{-2} s^{-1}), snow column organic carbon (kg m^{-2}), BC+dust SDE (W m^{-2}). All cycles are normalized for this comparison. Colors represent the Rocky Mountains (orange), the Tibetan Plateau (purple), the Arctic (green), and the Antarctic (maroon).

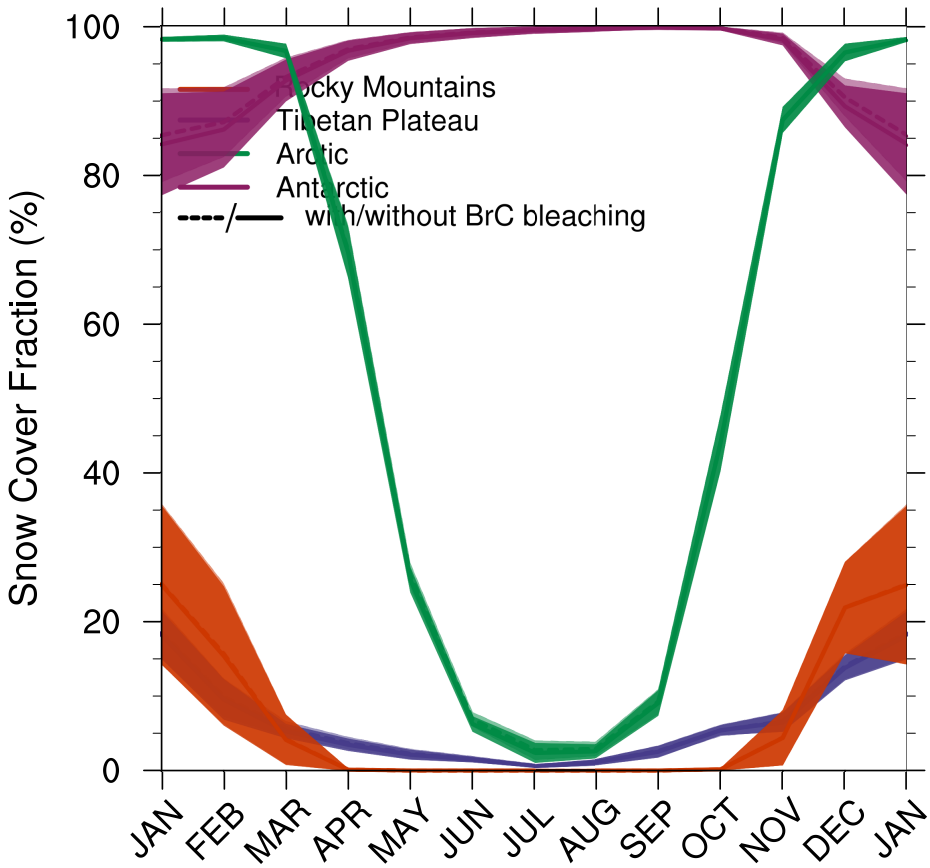

Figure S11. Monthly mean variation in 10-year mean snow cover fraction (%) from the four regions described in Fig. 8, ± one standard deviation. Colors represent the Rocky Mountains (orange), the Tibetan Plateau (purple), the Arctic (green), and the Antarctic (maroon). The snow cover fraction is from the BRC and BRC_PB simulations

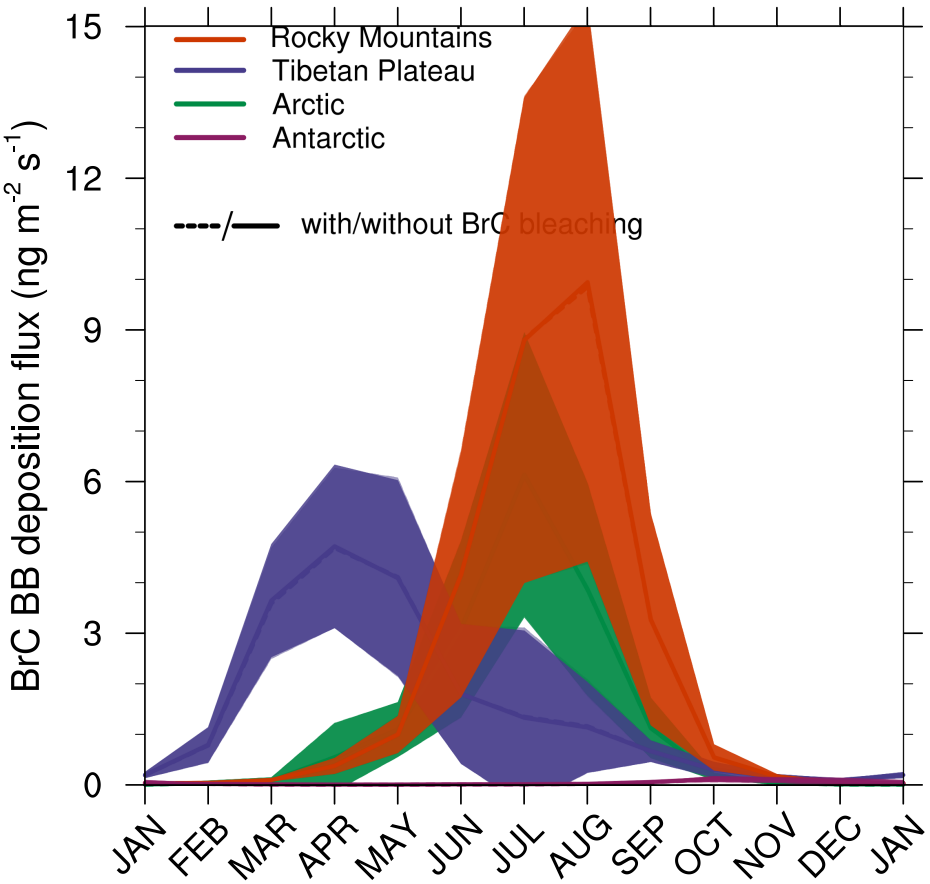

Figure S12. Monthly mean variation in 10-year mean BB BrC deposition flux (ng m^{-2} s^{-1}) from the four regions described in Fig. 8, ± one standard deviation. Colors represent the Rocky Mountains (orange), the Tibetan Plateau (purple), the Arctic (green), and the Antarctic (maroon). The deposition flux is from the BRC and BRC_PB simulations.

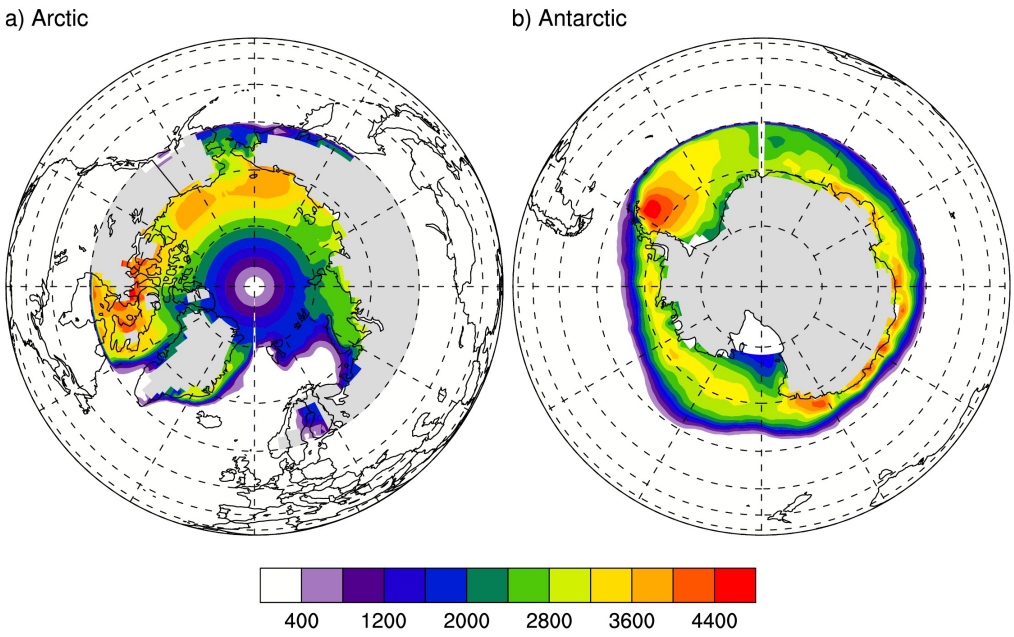

Figure S13. The 10-year mean sea-ice grid cell surface area (km^2) over (a) the Arctic and (b) the Antarctic.

	Observations	BRC
Canada and Alaska[a]		
Canadian Arctic	9.39±3.23	20.2±9.56
Canadian subarctic	15.42±8.64	24±7.73
N. Alaska Coast	9	54.14
Ellesmere Island	12	5.37
Greenland[a]		
South Greenland	1.1	–
Central Greenland	2	5.06
Northeast Greenland	7.53±10.88	–
Northwest Greenland	4.2	6.35
Greenland AWS	3.56±1.79	6.23±1.49
Russia[a]		
Western Russia	78.5±105.5	232.6±117.92
Eastern Russia	49.55±42.83	79.14±40.3
Svalbard and Norway[a]		
Svalbard	12.83±5.27	5.22±2.76
Norway	25±8.49	42.32±8.07
North America[b]		
Pacific Northwest	52.5±69.24	35.36±57.61
Intermountain Northwest	34±21	8.97±6.05
North U.S. Plains	46.53±66.82	51.11±54.23
Canada	19.14±13.38	155.31±8.57
China[c]		
Qilian Mountains	–	305.09±230.19
Inner Mongolia	300.67±22.03	471.36±121.43
Northeast Industrial	1393.33±1082.05	2088.18±1229

[a] Doherty et al. (2010)

[b] Doherty et al. (2014)

[c] X. Wang et al. (2013)

Table S1. Comparison of observed and modeled snow surface black carbon concentration (C^{est}, ng g^{-1}). Observations are from Doherty et al. (2010), Wang et al. (2013), and Doherty et al. (2014), and model results are from the BRC simulation. Here, "AWS" indicates samples taken from Automatic Weather Sites. When more than one sample is present, we include ±1 standard deviation of the sample group. Missing model data indicates lack of snow cover in the simulation. Missing observation data from Quilan Mountains is due to near 0 BC mass concentration.

	Observations	NOBRC	BRC_PB	BRC
Canada and Alaska[a]				
Canadian Arctic	42.65±7.0	39.68±9.2	51.23±6.81	64.0±6.57
Canadian subarctic	42.54±5.79	36.32±16.4	43.57±12.83	52.65±9.78
N. Alaska Coast	53	19.88	39.23	56.25
Ellesmere Island	61	34.01	39.67	47.91
Greenland[a]				
South Greenland	33	–	–	–
Central Greenland	51	35.74	46.02	58.86
Northeast Greenland	45.33±16.2	–	–	–
Northwest Greenland	47	49.26	57.41	70.38
Greenland AWS	47.57±6.32	41.38±6.68	50.71±7.25	63.55±8.38
Russia[a]				
Western Russia	24.25±3.95	8.81±8.06	19.19±17.26	28.51±26.1
Eastern Russia	40.64±8.46	28.01±6.77	48.43±4.6	64.14±8.49
Svalbard and Norway[a]				
Svalbard	28.83±4.36	37.07±3.24	45.16±2.61	53.41±6.04
Norway	24±2.83	17.51±0.37	35.48±0.18	50.0±3.78
North America[b]				
Pacific Northwest	22.5±6.19	–	19.67±19.69	30.28±44.71
Intermountain Northwest	35.88±16.41	55.98±31.17	64.63±23.03	72.05±13.64
North U.S. Plains	61.88±22.05	48.58±41.3	57.21±29.23	62.55±15.13
Canada	47.29±13.85	24.66±29.4	37.59±21.61	44.71±15.94
China[c]				
Qilian Mountains	~100	–	8.57±0.93	21.5±4.68
Inner Mongolia	47.3±9.29	–	51.92±20.85	50.79±20.92
Northeast Industrial	30.33±8.5	–	1.87±1.28	4.37±0.63

[a] Doherty et al. (2010)
[b] Doherty et al. (2014)
[c] X. Wang et al. (2013)

Table S2. Comparison of observed and modeled fractional contribution to non-BC aerosol light absorption ($f_{est,\,\%}$). Observations are from Doherty et al. (2010), X. Wang et al. (2013), and Doherty et al. (2014). Here, "AWS" indicates samples taken from Automatic Weather Sites. Model simulations are described in Table 2, and model f_{est} is (OC SDE + dust SDE) / Total Aerosol SDE. When more than one sample is present, we include ±1 standard deviation of the sample group. Missing data indicate lack of snow cover in the model simulation or snow cover strongly darkened by BC leading to unphysical values for model SDE.

Region	Land Area (km^2)	Sea-Ice Area (km^2)	Sea-Ice / Land Area
Arctic	1.86×10^7	1.19×10^7	0.64
Antarctic	1.42×10^7	1.06×10^7	0.74

Table S3. Comparison of land and sea ice surface areas in the Arctic (60˚N–90˚N) and Antarctic (60˚S–90˚S) receptor regions (Fig. 7). Land area is calculated by multiplying land fraction by grid-cell surface area. Sea-ice fraction is calculated by multiplying grid-cell sea-ice percentages by grid-cell surface area (Figure S12).